Summer 2012

Plastic strain accommodation and acoustic emission during melting of embedded indium particles in aluminum

Michael M. Kuba

Department:

PLASTIC STRAIN ACCOMMODATION AND ACOUSTIC EMISSION DURING MELTING OF EMBEDDED INDIUM PARTICLES IN ALUMINUM

by

MICHAEL MASAO KUBA

A THESIS

Presented to the Faculty of the Graduate School of the

MISSOURI UNIVERSITY OF SCIENCE AND TECHNOLOGY

In Partial Fulfillment of the Requirements for the Degree

MASTER OF SCIENCE IN METALLURGICAL ENGINEERING

2012

Approved by

David C. Van Aken, Advisor
Wayne Huebner
Matthew J. O'Keefe

PUBLICATION THESIS OPTION

This thesis has been prepared in the form of two manuscripts for publication. Pages 6–18 were published 15 June 2012 in Materials Letters, volume 77, pp. 89–92. Pages 19–47 will be submitted for publication in Metallurgical and Materials Transactions A. The Introduction and Appendices provide supplemental information to certain experimental procedures and calculations.

ABSTRACT

Melting of micron-sized (0.2 to 3 μm diameter) indium particles embedded in an aluminum matrix was discovered to produce acoustic emission. Melting of embedded immiscible particles produces a pure dilation during the phase transformation and has no long-range diffusion field to control the speed of transformation. It was found that acoustic emission can no longer be considered as a criterion of displacive transformations and that melting of micron-sized embedded particles is strain energy controlled. Acoustic emission was confirmed to result from the rapid relaxation of aluminum around indium particles embedded on grain boundaries. Prismatic punching of dislocation loops is proposed as the mechanism for volume accommodation during melting of the embedded indium particles. The resulting dislocation density was calculated to range between 3.5 x 10^8 and 4.1 x 10^9 cm^{-2}. Prior thermal history was found to affect the acoustic emission during melting of the embedded particles, and all effects could be explained in terms of a dislocation model. Analysis following the Eshelby inclusion model shows that acoustic emission and strain-controlled transformations are expected for particles 0.1 to 18 μm in diameter. It is suggested that any phase transformation associated with a volume change and matrix relaxation may generate acoustic emission when the transformation occurs rapidly enough. It is also suggested that liquid inclusions act as a free surface within higher-melting point matrices and facilitates dislocation nucleation.

ACKNOWLEDGMENTS

I wish to express my extreme gratitude to Dr. David C. Van Aken for his instruction, guidance, and patience during the course of my education. Were it not for him, I could not have found new limits on my intelligence and motivation. It is through the opportunities he has provided me that I hope to make an impact on the science of metallurgy. Funding from the National Science Foundation, the Department of Energy, and the American Iron and Steel Institute made this research possible under contract No. CMMI 0726888.

Dr. Wayne Huebner and Dr. Matt O'Keefe have been instrumental in my education and efforts in materials engineering. Dr. Huebner has instilled in me the joy of engineering research, and shown me that expressing wonder at the world around us should never grow old. Dr. O'Keefe was instrumental in setting the foundation of my metallurgical education both in lecture and by providing me my first research opportunities.

I also thank the entirety of the faculty, staff, and students in Materials Science and Engineering. They have shown me that good research truly is a group effort, and that advancement of human accomplishments would not be possible without people with a wide variety of backgrounds. In particular, Mr. Nathan Inskip, Mr. Jack Jones, and Dr. Simon Lekakh helped me become a much more practical engineer. The DSC work could not have been accomplished without the Materials Research Center, in particular Dr. Eric Bohannan. I could not have accomplished my goals without the aid of Ms. Amy Moore, Ms. Denise Eddings, Ms. Joyce Erkiletian, and Ms. Teneke Brown. Further, Mr. Sam Buckholz, Mr. Tony Wilshire, Ms. Laura Bartlett, and Ms. Krista Kalac provided a strong sounding board for both research and life decisions. Mr. Brandon Ensor, Mr. Tyler Preall, Mr. Joey Brookshire, Mr. Dan Broecker, and Mr. Zach Henderson have allowed me to practically be in two places at once in my research.

Through all of this, I owe the most to my wife, Liz Kuba. It is her encouragement and patience that has maintained my sanity and effort during the last two years. I simply cannot repay my debt to her, and am grateful for her love and commitment.

TABLE OF CONTENTS

Page

PUBLICATION THESIS OPTION iii

ABSTRACT iv

ACKNOWLEDGMENTS v

LIST OF ILLUSTRATIONS viii

LIST OF TABLES x

SECTION

1. INTRODUCTION 1

1.1. BACKGROUND 1

1.1.1. Acoustic Emission. 1

1.1.2. Melting of Embedded Particles. 2

1.2. PURPOSE AND OBJECTIVE 3

1.3. DEVELOPMENT OF APPARATUS 4

PAPER

I. PLASTIC STRAIN ACCOMMODATION AND ACOUSTIC EMISSION DURING MELTING OF EMBEDDED PARTICLES 6

ABSTRACT 7

1. INTRODUCTION 7

2. MATERIALS AND METHODS 9

2.1. Materials preparation. 9

2.2. Acoustic emission testing. 10

3. RESULTS 11

3.1. Microstructure characterization. 11

3.2. Acoustic emission. 12

4. DISCUSSION 13

5. CONCLUSIONS 17

ACKNOWLEDGMENTS 18

II. ANALYSIS OF ACOUSTIC EMISSION DURING THE MELTING OF EMBEDDED INDIUM AND ALUMINUM: A STUDY OF PLASTIC STRAIN ACCOMMODATION DURING PHASE TRANSFORMATION 19

ABSTRACT 20

I. INTRODUCTION 20

II. EXPERIMENTAL PROCEDURE 24

III. RESULTS 27

IV. DISCUSSION 36

V. CONCLUSIONS 46

ACKNOWLEDGMENTS 47

SECTION

2. CONCLUSIONS 48

APPENDICES

A. LABVIEW CODE FOR ACOUSTIC EMISSION APPARATUS 49

B. SPHERICAL ESHELBY INCLUSION SOLUTION 55

C. DISLOCATION DENSITY CALCULATION 60

D. DISLOCATION DENSITY MEASUREMENT BY XRD 63

BIBLIOGRAPHY 67

VITA 72

LIST OF ILLUSTRATIONS

Figure Page

PAPER I

1. Secondary electron images of the four Al–In compositions studied. 11

2. Average signal level detected versus temperature for each composition studied. 15

3. Average AE signal level of the Al-17In alloy compared with the corresponding DSC plot in heating at 0.17 C°/s 16

4. Average AE signal level of the Al-17In alloy compared with the corresponding DSC plot in cooling at 0.08 C°/s. 17

PAPER II

1. Acoustic emission and acoustic energy in as-cast aluminum-indium alloys as a function of composition..... 23

2. A comparison between internal friction (bottom) and DSC (top) of an Al-16In specimen. 24

3. Particle count as a function of volume as measured via serial sectioning. 28

4. The three-dimensional reconstruction of the area selected for serial sectioning..... 29

5. Optical (etched with Barker's reagent) and SEM micrographs of the Al-In conditions studied. 31

6. A comparison of DSC (line) and AE (scatter) for the first and second heating cycles of the intermediate-grained specimen. 32

7. A comparison of DSC (line) and AE (scatter) for the first and second heating cycles of the large-grained specimen. 33

8. A comparison of DSC (line) and AE (scatter) for the first and second cooling cycles of the large-grained specimen. 34

9. A comparison of DSC (line) and AE (scatter) in heating for the low-temperature anneal specimens. 35

10. A summary of the acoustic energy as a function of fraction particles at grain boundaries. 35

11. DSC of a melt-spun Al-12In alloy. 36

12. Activation energies for the nucleation of various vacancy sinks as a function of vacancy supersaturation.. 40

LIST OF TABLES

Table Page

PAPER I

1. The area percentage analysis and converted weight percentage of the cast alloys. .. 12

PAPER II

1. Metallographic measurements of microstructural features of the castings. 29

1. INTRODUCTION

1.1. BACKGROUND

1.1.1. Acoustic Emission. The bulk of this work is based on the acoustic emission (AE) technique. Elastic strain waves propagating through a material as a consequence of rapid energy release produce AE [1]. ASTM E 1316 describes two types of AE: a discrete detection called a "burst" emission, and a "continuous" emission usually consisting of several overlapping "burst" emissions creating a sustained signal [1].

Displacive solid-state transformations exhibit AE; literature ascribes the emission to the shear mechanism of transformation often observed for the martensitic transformation, which results in continuous emission [2]. Diffusion-based phase changes are said to transform too slowly to generate AE [2]. In steels, transformations to allotriomorphic ferrite or pearlite do not generate AE [2], but transformations to martensite [2] and bainite [3] do. Some sources define detection of AE during solid-state phase transformations as indicative of displacive or martensitic-like qualities where the phase transformation involves the military-like motion of dislocations that transforms the parent phase to the product phase [4].

AE can also be detected for melting/solidification events as the material contracts [5], e.g. bulk indium only exhibits AE upon solidification, but bulk antimony produces AE upon melting. There is debate in literature over the exact cause of the AE during melting or solidification events [6]. Frictional noise between solid crystals [7] and cluster addition/subtraction from the solid-liquid interface [8] have been presented as possible

explanations; however, the bulk of the detected phenomena may be as simple as the casting separating from the mold wall.

AE is also used to detect other rapid-energy release events in materials, such as dislocation creation and movement [9], dislocation multiplication at the upper yield point in steel, and ductile fracture processes during tensile testing [10,11]. Mechanical twinning (as demonstrated by the "crying" of tin when deformed) and cleavage fracture also generate AE, but typically as a burst emission [12]. The unique characteristics of AE detection mean that the technique often complements other measurements to improve characterization methods.

1.1.2. Melting of Embedded Particles. Embedding small particles (nano- or micro-sized) in a higher melting point matrix is known to alter the melting temperature of the particles [13,14]. Characterization of the melting point distribution of the embedded particles can be accomplished with differential scanning calorimetry (DSC) by monitoring heat flow with respect to temperature. Micron-sized (0.2 to 3 μm) indium particles usually exhibit two separate distributions, one melting at the equilibrium temperature of 156 °C, the other melting at an elevated temperature (~6 C° superheat) [13]. Conversely, nano-sized particles (less than 100 nm diameter) often exhibit both melting point elevations and depressions in the same specimen [14].

Literature provides several explanations for changes in melting temperature, including strain energy effects [15,16], interfacial energy effects [17-19], and kinetic barriers to nucleation [20]. Strain energy is usually neglected for particles less than 100 nm in diameter, which suggests interfacial energy or atomic ordering effects at the interface as the cause for the change in melting temperature [17-19]. Rösner et al. noted

that the particle morphology (i.e. faceted or curved) influences whether the particle melts above or below the equilibrium melting temperature for lead in aluminum [14].

Conversely, strain energy becomes important for micron-sized particles as studied by Malhotra and Van Aken [13, 21-22], who used internal friction and DSC to characterize the melting of indium particles 1 to 20 μm in diameter and embedded in an aluminum matrix. Correlation of internal friction, DSC, and calculations showed that the aluminum matrix resisted the 2.5% volume expansion of the melting indium particles and resulted in a longer relaxation time (and subsequently higher temperature) for melting particles at low angle boundaries or within grains. Neither internal friction peaks nor superheating was observed for laminated specimens of aluminum and indium and Malhotra and Van Aken concluded that the indium was not fully constrained by the matrix [22].

1.2. PURPOSE AND OBJECTIVE

Bainite and martensite are known to produce acoustic emission upon transformation [3]; it is believed that the shearing transformation mechanism in martensite generates the AE [2] and that detection of AE for bainitic transformations implies a similar transformation mechanism [23]. In addition, both transformations result in a high dislocation density on the order of 1.7×10^{10} cm^{-2} for continuously cooled bainite and 7×10^{11} cm^{-2} for martensite (M_S = 300 °C) [23]. Most researchers associate the AE with the shear transformation; however, the production of a high dislocation density may in fact be separate from the shear transformation and created by plastic accommodation of a volume change. Successful AE detection of a phase transformation known to be purely dilatational but also known to result in dislocation creation would

provide the desired test. The work reported in this thesis was based upon the hypothesis that melting of micron-sized embedded particles in a higher melting point matrix might result in the desired transformation, and that the stress conditions around a particle as it expands upon melting are similar to the conditions during void nucleation and growth during ductile fracture (i.e. hydrostatic stresses). Consequently, detection of AE would also support the argument by some metallurgists that bainite is a diffusive reaction [24] and that AE detection is not necessarily indicative of a displacive reaction.

1.3. DEVELOPMENT OF APPARATUS

A dedicated AE measurement computer was purpose-built for the thesis studies. A two channel acoustic emission system on a PCI-card was purchased from Physical Acoustics Corporation and installed in a Dell Optiplex GX270. A switchable 20/40/60 dB gain preamp with a 100-1200 kHz band-pass filter was coupled with a Micro-30 Navy Type V PZT piezoelectric transducer to detect AE.

A program was written in National Instruments LabVIEW software to process the signals obtained by the PCI card. The LabVIEW program obtained specimen temperature data from an NI 9219 interface through an NI USB-9162 converter, and recorded temperature and AE data with respect to time. Documentation of the program can be found in Appendix A.

Aluminum-indium specimens were machined to right cylinders with three orthogonal holes drilled through the specimen and each normal to a surface. Specimens were nominally 12.7 mm tall and either 13 or 14.3 mm in diameter depending on the mold used to cast the specimens. The holes drilled were nominally 4.8 mm in diameter. This specimen design was chosen to minimize thermal gradients in the specimen while

still providing enough transformative volume for good detection of the AE signal. Specimens were attached by high-temperature epoxy to a 6061 aluminum rod used as a waveguide, which was mounted to a cross-member to suspend the specimen in a molten salt bath. The piezoelectric transducer was clamped to the other end of the waveguide so that it was not exposed to the bath temperature. Dow Corning high vacuum grease was used as a couplant.

PAPER

I. PLASTIC STRAIN ACCOMMODATION AND ACOUSTIC EMISSION DURING MELTING OF EMBEDDED PARTICLES

Michael M. Kuba, David C. Van Aken

Materials Science and Engineering

Missouri University of Science and Technology

223 McNutt Hall, 1400 N. Bishop, Rolla, MO 65409-0330, USA

Tel.: 573-341-4717

Email: dcva@mst.edu

Keywords: Acoustic emission, Dislocation generation, Melting, Phase transformation, Strain accommodation

Published in Materials Letters, volume 77, 15 June 2012, pp. 89-92

ABSTRACT

Melting point phenomena of micron-sized indium particles embedded in an aluminum matrix were studied by means of acoustic emission and differential scanning calorimetry. The acoustic response measured during melting increased with indium content. Correlations with differential scanning calorimetry suggest that large indium particles or particles at grain boundaries generate the greatest acoustic emission. Acoustic emission during melting suggests a dislocation generation mechanism to accommodate the 2.5% volume strain required for melting of the embedded particles.

1. INTRODUCTION

Embedding small particles of a lower melting phase in a higher melting point matrix is known to increase the melting temperature of the particles. Numerous causes for the phenomenon have been proposed, including strain energy effects [15-16], interfacial energy effects [17-19], and kinetic barriers to nucleation [20]. Studies suggesting interfacial energy or atomic ordering effects at the interface [17-19] as the cause of melting temperature elevation only consider nanometer-sized particles and ignore strain energy effects. These nanometer-sized particles often have strongly faceted shapes with close packed planes forming the interfaces or facets. The nanometer sized particles show a melting point depression in cases where the interface is disturbed with a nonfaceted boundary [14].

Malhotra and Van Aken studied the anelastic strain accommodation during melting and solidification of micron-sized indium particles embedded in an aluminum matrix [13,21,25]. By measuring internal friction and performing differential scanning calorimetry (DSC), they concluded that the observed increase in melting temperature of

the micron-sized indium particles was mainly a strain energy effect of the matrix resisting the volume change during melting or solidification. The strength of the internal friction peak was frequency and temperature rate dependent suggesting that the anelastic effect was associated with a matrix relaxation mechanism related to the volume change upon transformation. Internal friction peaks were also observed upon cooling and three peaks were observed in both internal friction and DSC experiments [21]. Internal friction peaks were not observed for laminated composite structures where the indium was not fully constrained by the matrix [22].

Acoustic emission (AE) describes the propagation of elastic waves resulting from rapid energy release in a material [1]. Two qualitative types of AE exist: “burst,” a discrete signal, and “continuous,” a sustained signal usually caused by several overlapping bursts [1]. For example, crack growth tends to generate a burst emission, while dislocation movements result in a continuous emission [12]. Phase transformations that generate AE usually exhibit continuous emission due to time or temperature dependent nucleation [12].

According to literature, displacive solid-state transformations exhibit AE; the shear mechanism or motion of dislocation arrays produces a rapid strain energy release that is detected as AE. Diffusive transformations occur too slowly for this effect [2]. In steels, formation of allotriomorphic ferrite or pearlite does not generate AE [2], but martensite [2] and bainite [3] formations do. Thus, AE has become a useful tool in determining the displacive or martensitic-like qualities of a solid-state transformation [4]. It should be noted that solid to liquid transformations also exhibit AE as the material contracts [5], e.g. indium would only exhibit AE upon solidification, but antimony would

produce AE upon melting. The exact cause of AE during melting and solidification is controversial [6], but has been explained as frictional noise between solid crystals [7] or cluster addition/subtraction from the solid–liquid interface [8].

AE techniques also detect other phenomena involving dislocation creation and movement [9], dislocation multiplication at the upper yield point in steel, and ductile fracture during tensile testing [10,11] . It is suggested here that the stress conditions around an indium particle during melting are similar to that required for void nucleation and growth during ductile fracture, i.e. the volume increase during melting may also be accommodated by dislocation generation and that this process may be reversible. Consequently, it was hypothesized that the melting of an embedded particle might generate AE.

The scope of this article is to show successful AE detection of the melting of indium particles embedded in an aluminum matrix. By investigating the nature of the reaction, a better understanding of both solid–liquid and solid-state transformations may be realized.

2. MATERIALS AND METHODS

2.1. Materials preparation. Bulk material for testing was prepared by melting aluminum in fireclay crucibles in a resistance furnace at 800 °C. Indium pieces were wrapped in aluminum and plunged into each melt to create a range of aluminum–indium alloys with nominal chemistries of 0, 4, 8, 12, and 17 wt.% indium. All materials used were at least 99.99% pure with respect to metal content. The melt was physically stirred to aid in homogenization since a liquid miscibility gap occurs in the Al–In system with a critical temperature at 875 °C. The alloys were chill cast into 13 mm diameter cylinders

using an aluminum mold. The microstructure was characterized using a Hitachi S-570 scanning electron microscope. DSC was also performed at a heating rate of 0.169 C°/s to confirm the presence of both equilibrium-melting particles and indium particles exhibiting elevated melting temperatures.

2.2. Acoustic emission testing. AE testing was performed on as-cast specimens, which were machined into right cylinders with three orthogonal holes drilled normal to the surfaces to produce a cylinder wall thickness of 4 mm. The three holes were drilled to reduce thermal gradients in the specimen. Specimen temperature was recorded from a thermocouple swaged into a 2.25 by 2.25 mm hole with machining chips of the same composition. A high temperature epoxy was used to attach the specimens to a 12.7 mm diameter aluminum alloy 6061 waveguide. A cross beam was mounted to the wave guide to suspend the specimen into a molten salt bath held at 200 °C. A PZT Navy type V transducer produced by Physical Acoustics Corporation was clamped to the fixture with Dow Corning high vacuum grease as a couplant. AE and specimen temperature were monitored using National Instruments LabVIEW software during heating and cooling. The specimen heating rate was measured to be 0.16 to 0.29 C°/s, while the cooling rate was 0.52 to 0.73 C°/s. AE was monitored by an average signal level measured in decibels with a time constant of 0.1 seconds, rather than by hit count, as used by Van Bohemen [26].

3. RESULTS

3.1. Microstructure characterization. Representative micrographs are shown in Figure 1. Three images of different areas for each composition were analyzed using ImageJ software to determine volume fraction of indium, which was converted to weight percentage using appropriate densities. Compositional results are shown in Table 1.

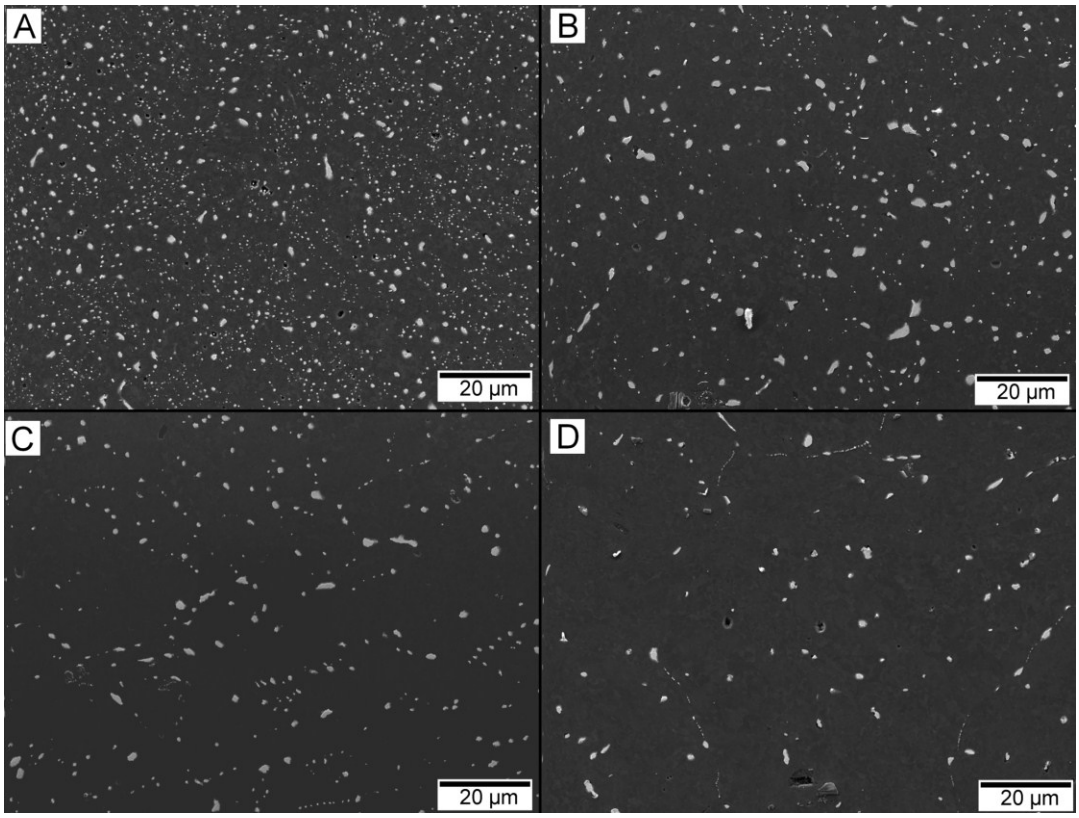

Figure 1. Secondary electron images of the four Al–In compositions studied. Micrographs show (A) 17 wt.% In, (B) 12 wt.% In, (C) 8 wt.% In, and (D) 4 wt.% In.

Table 1. The area percentage analysis and converted weight percentage of the cast alloys.

Nominal composition	Area percentage indium	Weight percentage indium	Average particle volume (μm³)
Al-17In	5.8	15.70	0.165
Al-12In	3.9	10.56	0.465
Al-8In	2.1	5.69	0.425
Al-4In	1.4	3.79	0.659

3.2. Acoustic emission. Typical plots of AE versus temperature for each alloy are shown in Figure 2. The pure aluminum specimen does not exhibit AE in the temperature range of interest. However, the aluminum–indium alloys do exhibit AE and the AE increases with increasing indium content.

The recorded heat flow from DSC of the cast alloys was similar to that reported by Malhotra and Van Aken [13]. The first peak was interpreted as indium particles on the grain boundaries melting at the equilibrium temperature, 156 °C [22]. The second peak represents elevated temperature melting within the grains [13]. A comparison in heating between the Al-17In AE curve and its corresponding DSC curve is shown in Figure 3. The heating rate for the AE curve was measured to be 0.165 C°/s. A comparison in cooling between AE and DSC is presented in Figure 4. The specimens were allowed to cool freely for both AE and DSC: the AE curve was measured to cool at 0.577 C°/s, compared to 0.079 C°/s for the DSC curve. In general, better results were obtained in cooling, but to differentiate the AE from that previously reported for solidification of the indium [5] it was necessary to first show that AE was detected for each specimen upon

heating. Interestingly, there appears to be three different populations of particles that give rise to AE upon solidification, whereas upon heating the AE appears to correlate best with particles melting near equilibrium. This may in fact be just a size effect since the larger indium particles are situated at grain boundaries; however, no correlation was found between indium particle size distribution as measured from Figure 1 and melting or solidification temperature distribution from DSC.

4. DISCUSSION

To the authors' knowledge, this is the first recorded detection of acoustic emission resulting from the melting of embedded particles. As such, determination of the source mechanism of the acoustic emission should cast light on the nature of the melting and previously reported internal friction. Diffusion and diffusive processes do not generate AE on their own [2], so any interfacial rearrangement related to atomic diffusion cannot be the source of the emission. Melting processes are not considered to be displacive transformations, so the AE cannot be a result of shear waves, as it is in martensitic transformations. No cracks are propagated as a result of indium particle melting, as these were not observed and the internal friction results obtained by Malhotra and Van Aken [13,21] would have detected them. In terms of bulk phase transformations, indium should only exhibit AE during solidification, but was observed here to occur upon both heating and cooling. Matrix dislocation motion and generation is the remaining microstructural source of the AE. Given that the matrix must accommodate a 2.5% volume change due to melting or solidification of the indium, local dislocation motion or creation must occur. A mechanism of dislocation relaxation is supported by the internal friction studies of Malhotra and Van Aken [22] and the observation of two melting

temperature distributions was explained by differences in relaxation times. Internal friction peaks were not observed for indium when unconstrained as shown for an Al–In laminate structure [21,22]. Indium particles situated at grain boundaries would have faster relaxation times and melt at equilibrium whereas indium particles embedded within the aluminum grains would be constrained by longer relaxation times and exhibit superheating. For AE to be observed the matrix relaxation must necessarily be rapid and this may explain the lack of AE for those particles melting at elevated temperatures. Relaxation times for particles observed in this study were calculated following Malhotra and Van Aken [13,22] . Particles situated at grain boundaries would have relaxation times on the order of 4×10^{-6} s. Conversely, particles melting at elevated temperatures have a much longer relaxation time on the order of 4×10^{5} s, which would preclude AE.

In contrast to melting, a stronger correlation between DSC and AE is observed upon cooling and it appears that all of the indium particles generate AE during solidification. Work by Koike et al. [27] and Huang et al. [28] suggests that liquid phase present in the parent material acts as a free surface and contributes to dislocation annihilation. It is interesting to speculate that the liquid–solid interface may also provide an easy dislocation emission source similar to a grain boundary or a free surface; thus a short relaxation time and generation of AE. Differences in AE upon heating and cooling may thus be explained by a difference in dislocation nucleation from solid indium particle interfaces versus a liquid interface. Upon solidification, the nature of the prismatic loop would also change from interstitial to vacancy or possible annihilation of interstitial loops previously generated on melting. It should be noted that Malhotra and

Van Aken did not consider dislocation generation as a possible relaxation mechanism to explain the observed internal friction peaks.

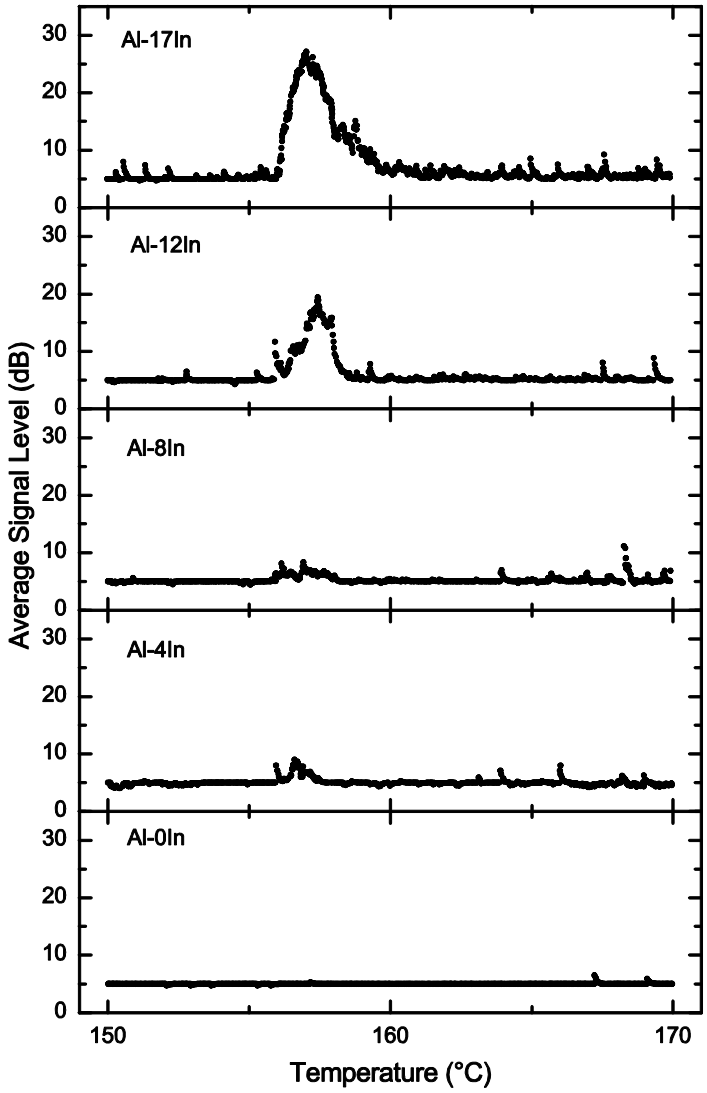

Figure 2. Average signal level detected versus temperature for each composition studied. Thermal lag was removed and the initiation of the AE peak was placed at 156 °C. A logarithmic smoothing algorithm was applied to reduce ambient noise.

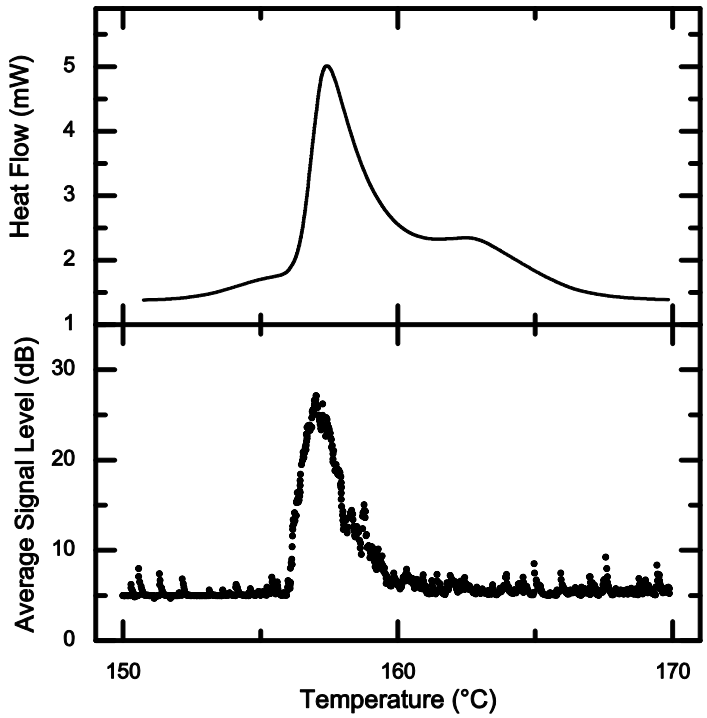

Figure 3. Average AE signal level of the Al-17In alloy compared with the corresponding DSC plot in heating at 0.17 C°/s.

Molecular dynamics simulation work and spall testing by D. C. Ahn et al. [29,30], and laser shock tests by Lubarda et al. [31] confirm interstitial prismatic loop emission as a viable mechanism for void growth during fracture at temperatures too low for diffusion to occur within the necessary time scale. Prismatic loop emission can be visualized as a dislocation loop of edge character on all sides being "punched" out from the particle, rather than growing to encircle the particle. It is this "punching" of interstitial plates that could produce the strain waves necessary for acoustic emission. It is worth mentioning that prismatic loops are approximately 75% the size of the void radius [29] and are emitted from the particle in a direction away from the particle and parallel to the Burgers vector. Indium particles situated at grain boundaries could emit these prismatic loops into one of the adjacent grains and these loops would not be constrained by the boundary or

the different grain orientations. It would also be expected that larger particles would generate more loops and produce greater AE. Future work will examine the size dependence of the AE.

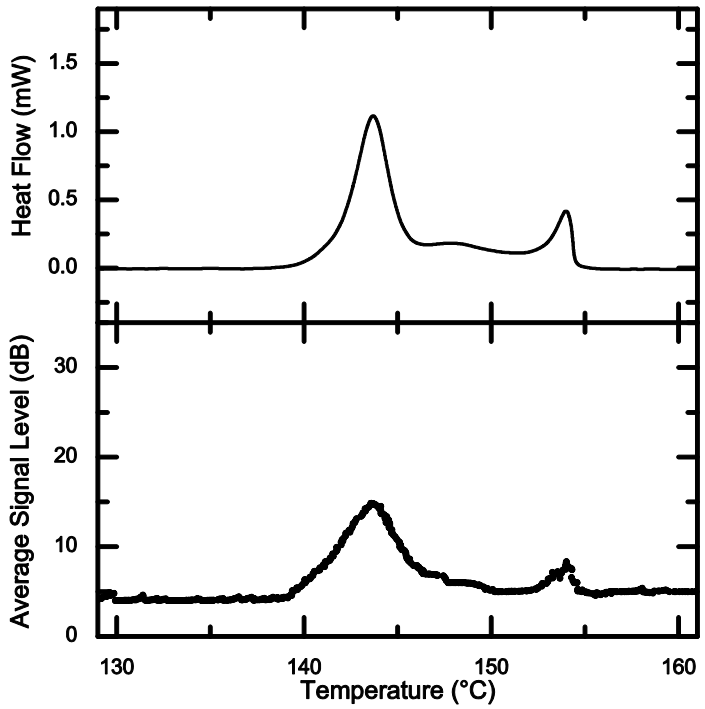

Figure 4. Average AE signal level of the Al-17In alloy compared with the corresponding DSC plot in cooling at 0.08 C°/s. Three distinct solidification distributions were also observed upon cooling by Malhotra and Van Aken in both DSC and internal friction [21].

5. CONCLUSIONS

In summary, this study shows that AE can be generated as a result of plastic strain accommodation by the matrix during the melting of an embedded particle. A dislocation mechanism of prismatic loop generation has been proposed. Further research is currently being conducted to characterize the AE relative to location, and size of the embedded

particle as well as the dislocation substructure of the aluminum matrix in generating the AE.

ACKNOWLEDGMENTS

This work was supported in part by the National Science Foundation, the Department of Energy, and the American Iron and Steel Institute under contract No. CMMI 0726888.

II. ANALYSIS OF ACOUSTIC EMISSION DURING THE MELTING OF EMBEDDED INDIUM AND ALUMINUM: A STUDY OF PLASTIC STRAIN ACCOMMODATION DURING PHASE TRANSFORMATION

Michael M. Kuba, David C. Van Aken

Materials Science and Engineering

Missouri University of Science and Technology

223 McNutt Hall, 1400 N. Bishop, Rolla, MO 65409-0330, USA

Tel.: 573-341-4717

Email: dcva@mst.edu

To be submitted for publication in Metallurgical and Materials Transactions A.

ABSTRACT

Acoustic emission is used here to study melting and solidification of embedded indium particles in the size range of 0.2 to 3 μm in diameter and to show that dislocation generation occurs in the aluminum matrix to accommodate a 2.5% volume change. The volume averaged acoustic energy produced by indium particle melting is similar to that reported for bainite formation upon continuous cooling. A mechanism of prismatic loop generation is proposed to accommodate the volume change and an upper limit to the geometrically necessary increase in dislocation density is calculated as 4.1×10^{9} cm^{-2} for the Al-17In alloy. Thermomechanical processing is also used to change the size and distribution of the indium particles within the aluminum matrix. Dislocation generation with accompanied acoustic emission occurs when the melting indium particles are associated with grain boundaries or upon solidification where the solid-liquid interfaces act as free surfaces to facilitate dislocation generation. Acoustic emission is not observed for indium particles that exhibit elevated melting temperatures, i.e. superheat. The acoustic emission work corroborates previously proposed relaxation mechanisms from prior internal friction studies and that the superheat observed for melting of these micron-sized particles is a result of matrix constraint.

I. INTRODUCTION

Recent study of the aluminum-indium system has shown that equilibrium melting of the indium particles can be detected by acoustic emission (AE) techniques [32]. AE results from rapid energy release that creates elastic waves in a material. According to literature, displacive solid-state transformations generate AE resulting from the shear mechanism of transformation. Diffusive transformations normally occur too slowly to

generate AE [2]. In steels, martensite [2] and bainite [3] generate AE, but formation of allotriomorphic ferrite or the eutectoid product pearlite does not [2]. Formation of Widmanstätten ferrite has been suggested to also generate AE [3]. Consequently, displacive or martensitic-like solid-state transformations are often distinguished from diffusion controlled phase transformations by the presence of AE [4]. However, liquid-solid transformations are also known to exhibit AE as the material contracts, i.e. most materials exhibit AE upon solidification but not melting [5]. The exact cause of solidification AE is debated [6], but may be due to frictional noise between solid crystals [7], cluster addition or subtraction from the solid-liquid interface [8], or perhaps casting separation from the mold wall. AE is detected in crystallizing polymers due to cavitation in areas of occluded liquid where shrinkage stresses overwhelm the cohesive strength of the melt [33]. Acoustic emission is also detected during tensile tests for dislocation creation and motion associated with an upper yield point [9] and for void nucleation during ductile fracture processes [10]. However, even a small amount of prior cold work has been shown to drastically decrease the AE response from dislocation movement in aluminum during tensile tests [9]. Presence or absence of AE in aluminum is dependent upon the slip distance and a maximum dislocation density of 2.34×10^{6} cm^{-2} for detectable AE is predicted for yielding [9]. Thus presence of AE during phase transformations provides powerful insight into the mechanism of the transformation because the sources of AE are well documented.

Malhotra and Van Aken [13] have proposed a strain energy effect associated with the 2.5% volume change upon melting for embedded indium inclusions in aluminum. The calculated increase in melting temperature (~6 C°) was in good agreement with superheat

measured by differential scanning calorimetry (DSC) and that observed by internal friction. Malhotra and Van Aken also demonstrated that the internal friction peaks observed during melting are dependent upon applied test frequency and heating rate; and as a result, a matrix relaxation process controls the degree of superheat [13]. Consequently, Kuba and Van Aken suggested that the stress conditions around an indium particle during melting are similar to that required for void nucleation and growth during ductile fracture [32]. The aluminum matrix was theorized to plastically accommodate the volume change of the melting indium particles and result in dislocation generation and motion. AE would be produced under these conditions when the matrix relaxes rapidly as calculated by Malhotra and Van Aken for indium particles sitting on grain boundaries [32]. The AE is duplicated in Figure 1 for reference. The AE detected is a function of indium content and the acoustic energy is plotted as the integral of the squared RMS voltage with respect to time.

Internal friction results from the work of Malhotra and Van Aken are shown in Figure 2 [13]. Two internal friction peaks were detected upon heating and three internal friction peaks were observed upon cooling. These melting and solidification events could be directly correlated with enthalpic changes observed using DSC. The two melting points detected were interpreted as a difference in diffusional relaxation times, but a dislocation generation model as suggested by Kuba and Van Aken to explain the AE was not considered. In contrast, the results of Wolfenden and Robinson [34] studying leaded brass produced only one internal friction peak at the melting temperature of lead. The strength of an internal friction peak should be noted to be dependent upon the product of test frequency and relaxation time. A maximum in the internal friction peak is obtained

when the product of the test frequency and the relaxation time is one. The lower test frequency used by Malhotra and Van Aken would be useful in probing diffusional relaxation mechanisms, while the 40 kHz test frequency used by Wolfenden and Robinson would be more likely to show the shorter relaxation time associated with dislocation generation mechanisms more typical of AE.

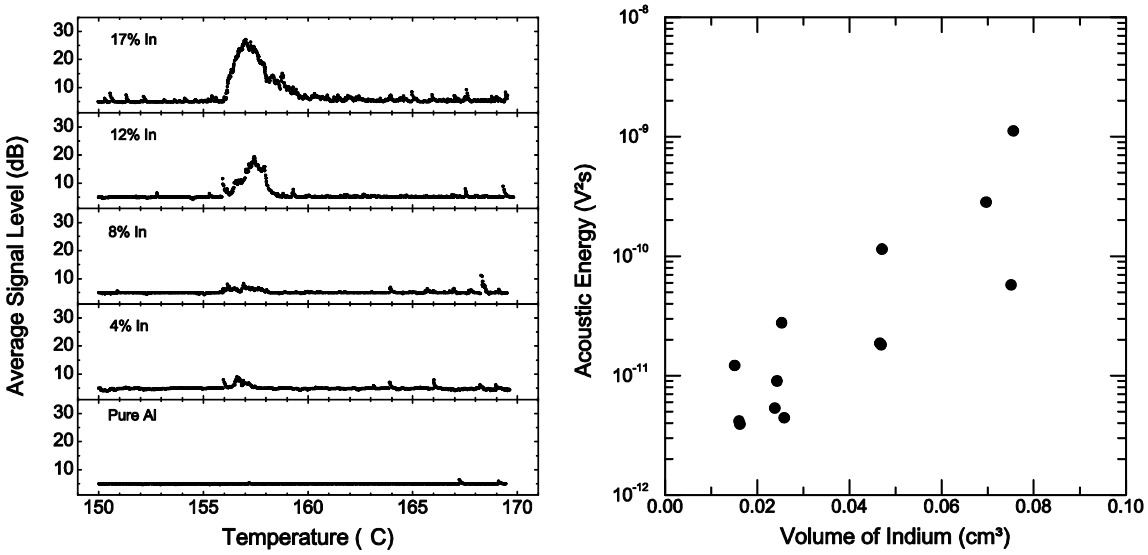

Figure 1. Acoustic emission and acoustic energy in as-cast aluminum-indium alloys as a function of composition. Left figure was originally published in Materials Letters [32].

The purpose of this study is to further investigate the nature of embedded particle melting, since melting or solidification transformations produce a simple dilation that is common to most phase transformations, but is not complicated by long range diffusion or motion of a solid-solid interface. Previous studies have shown melting temperature to be dependent on particle location [13]; particles on grain boundaries melt at the equilibrium

temperature, while particles embedded within aluminum grains melt at elevated temperatures. The current study investigates thermomechanically processed aluminum-indium alloys to show the effect of decreasing the number density of particles sitting on grain boundaries and observing the changes in AE. The study aims to further compile evidence of a dislocation-based relaxation of the volume strain associated with phase transformations.

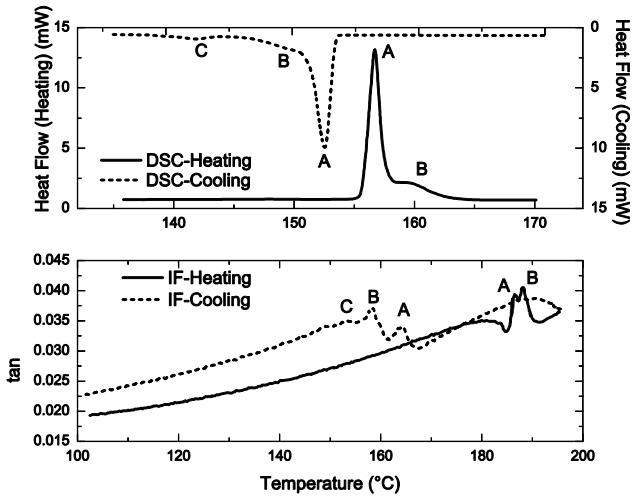

Figure 2. A comparison between internal friction (bottom) and DSC (top) of an Al-16In specimen.

II. EXPERIMENTAL PROCEDURE

Aluminum specimens with nominal 17 wt.% indium additions were chosen for this study, since the composition is close to the monotectic composition and solidification produces a large number density of embedded indium particles. Compositions greater than 17.4 wt.% indium would result in liquid phase separation and a bimodal particle size

distribution. Aluminum shot was melted in a fireclay crucible using a resistance furnace at 820 °C. Aluminum-wrapped indium pieces were plunged into each melt and physically stirred for homogenization as liquid miscibility is possible at 820°C. Both materials were at least 99.99% with respect to metal content. The melts were chill cast into 13 mm and 14.3 mm diameter cylinders using aluminum molds.

The 13 mm diameter cylinders were sectioned to 13 mm tall specimens and compressed to induce 5 to 6 percent plastic strain. The specimens were recrystallized at 500°C for one hour to produce larger grain sizes [35] where most of the indium particles will be within the grains. The as-cast condition produced the highest indium concentration on grain boundaries. To study an intermediate condition, the 14.3 mm diameter cylinders were swaged to 12.7 mm to induce 20% strain. The cylinders were recrystallized at 250 °C for 1 hour to produce a recrystallized grain structure between the as-cast and large-grained specimens [35]. Specimens for optical microscopy were polished using standard metallographic procedures and electrochemically etched with Barker's reagent (1.8% HBF_4 in water) at 30 VDC. Five locations were used to determine grain size using Jeffries' planimetric method. The microstructure was further studied using a Hitachi S-570 scanning electron microscope. Five images per sample configuration were analyzed using ImageJ software to determine indium fraction and particle size. DSC was also used to characterize the melting phenomenon under study. Particle size was also investigated on the Al-17In alloy previously reported on in Materials Letters [32]. A volume of dimensions 14 μm x 17 μm x 19 μm was examined by serial sectioning using a focused ion-beam SEM. Gallium ions were used to ion-mill

the alloy. The serial sectioning micrographs were aligned and recomposed into a three-dimensional volume using Avizo 7 software.

An additional batch of aluminum with 17% indium was chill cast in the 14.3 mm diameter mold to provide the as cast condition and to investigate the effect of cold work and low-temperature annealing on the possible dislocation structures produced during melting and solidification. Select specimens were annealed at 140 °C for two hours or swaged to 12.7 mm and annealed at 140 °C for two hours. The annealing temperature was chosen such that the indium particles would not melt during the heat treatment, but dislocation structures would recover [36]. Some specimens were also retained to test the as-cast condition for this batch. DSC and metallography were performed as mentioned above.

AE testing was performed on specimens machined to right cylinders with three orthogonal holes drilled through the specimen and normal to the surfaces. A wall thickness of 4 mm was produced in order to minimize thermal gradients in the specimen. Temperature was recorded using a type K thermocouple swaged into a 2.25 x 2.25 mm hole with machining chips of the same composition for each specimen. The specimens were attached to 12.7 mm diameter aluminum alloy 6061 waveguides by a high temperature epoxy. For each test, a cross beam was mounted to the wave guide to suspend the specimen in a salt bath held at 200°C. A PZT Navy type V transducer produced by Physical Acoustic Corporation was clamped to the end of the waveguide with Dow Corning high vacuum grease as a couplant. A virtual instrument designed in National Instruments LabVIEW software was used to record the AE signal and temperature simultaneously. After heating to the salt bath temperature, select specimens

were removed from the salt bath and allowed to cool while still monitoring AE and temperature. AE was measured as an average signal level with a time constant of 0.1 seconds as used by Van Bohemen [26]. Time-averaged AE data can be related to the energy of the transformation in a manner similar to DSC, and can be a better measure of continuous emission when the amplitude is low but the event occurrence rate is high. Specimens were subjected to a second heating and cooling cycle while AE was monitored, but with a 20 minute hold after heating to observe possible annealing effects. Thermal lag was removed from the AE plot by shifting the onset of AE in heating to the equilibrium melting temperature and upon cooling by direct comparison with DSC results. AE plots were exponentially smoothed to filter out noise.

Melt-spun aluminum with 12 wt.% indium alloy was also prepared to investigate the differences between indium nanoparticles and the micron-sized particles obtained during chill casting. DSC was performed to observe any differences in melting.

III. RESULTS

Particle size analysis from the serial section is shown in Figure 3 and is compared to prior results. A single particle size distribution ranging from 0.2 μm to 3 μm in diameter was observed. In contrast, the DSC results show two distinct populations with different melting temperatures. Thus, the melting behavior is not produced by two different size distributions. The shape of the indium particles was determined by examining the aluminum cavities that were reconstructed. Indium was liquated during ion milling since the gallium alloyed with the indium to produce melting of the indium particles. The eutectic for indium and gallium is at 15.7°C. Consequently, minor pore broadening may have occurred. No particle faceting could be discerned from the cavity

and internal voids with in the indium would have been indistinguishable from those created by liquation. An image of the three dimensional reconstruction is shown in Figure 4.

Area fraction analysis of SEM images of the as-cast cross-section resulted in 15.6 wt.% indium content for the cast material. Results from quantitative metallography are presented in Table 1; uncertainties listed are at 95% confidence levels. Representative optical and secondary electron micrographs are shown in Figure 5. Smaller grain size correlates with more grain surface area, and it can be seen that the fraction of particles on the grain boundaries increases as grain size decreases.

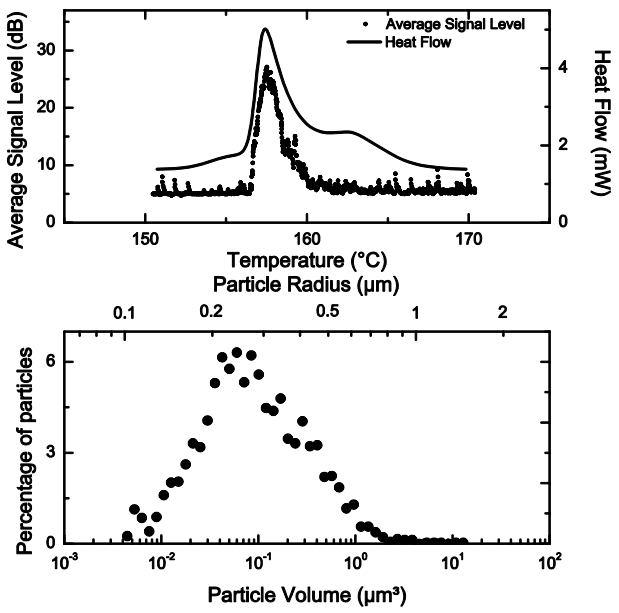

Figure 3. Particle count as a function of volume as measured via serial sectioning.

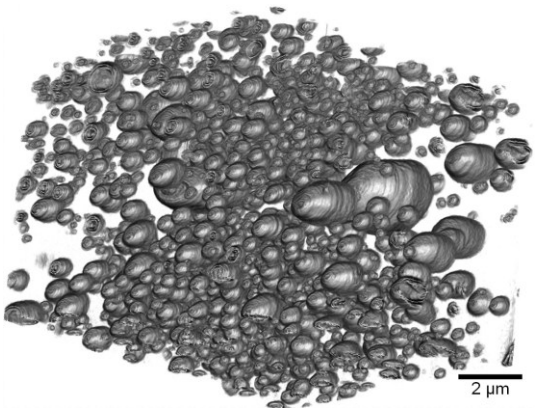

Figure 4. The three-dimensional reconstruction of the area selected for serial sectioning.

Table 1. Metallographic measurements of microstructural features of the castings.

	Average Particle Diameter (µm)	Aluminum Grain Surface Area per Unit Volume (mm^{-1})	Area Fraction of Particles at Grain Boundaries
As-cast	1.16 ± 0.06	10.7 ± 1.6	0.33
Intermediate-grained	1.00 ± 0.02	11.5 ± 0.9	0.25
Large-grained	1.38 ± 0.04	7.54 ± 0.72	0.13

Characteristic AE and DSC comparisons for heating the two recrystallized grain size configurations are shown in Figure 6 and Figure 7. Two peaks are present in the DSC in heating; one near the equilibrium melting temperature of 156 °C [37], while a broader elevated-temperature peak partially overlaps the first. Indium particles on the grain boundaries are expected to melt at the equilibrium temperature and produce AE during rapid matrix relaxation. Consequently, the intermediate-grained specimens in Figure 6 show more AE than the large-grained specimens in Figure 7. The DSC for the intermediate-grained specimens correlates to the AE data, as both the equilibrium melting

peak height and the AE peak increase for the second cycle. The large-grained specimens follow an opposite trend: the equilibrium peak height increases while the AE peak decreased for the second cycle. It may be worth considering that the large-grained specimens were quenched in water from 500 °C during the heat treatment to speed handling time. The possible effects of quenching on the AE and DSC will be examined in the discussion.

The large-grained specimens were also monitored in cooling for both AE and DSC, as seen in Figure 8. Several peaks were present in both the AE and DSC in cooling. Good AE-DSC peak temperature correlation was obtained for the large-grained specimens, with the two lowest temperature peaks coalescing into one single low-temperature solidification peak after the 20 minute hold at 200 °C. The relationship between the height of the AE and DSC peaks in cooling is not constant. While the DSC peaks are relatively similar in height on the first cycle, the AE is strongest for the two most undercooled peaks.

The as-cast AE response is shown in Figure 9 and demonstrates a larger peak than the intermediate-grained specimens. Low-temperature annealing experiments were performed to investigate matrix recovery (elimination of point defects and dislocation recovery) in determining the DSC and AE characteristics. AE and DSC comparisons for the low-temperature annealing test specimens are also shown in Figure 9 and are compared to the as-cast specimen. The 140 °C anneal did not significantly change the DSC response in heating, but did increase the AE peak. Cold working the specimen followed by the annealing treatment is seen to decrease the AE relative to the as cast condition, but increases relative to the height of its own equilibrium melting DSC peak.

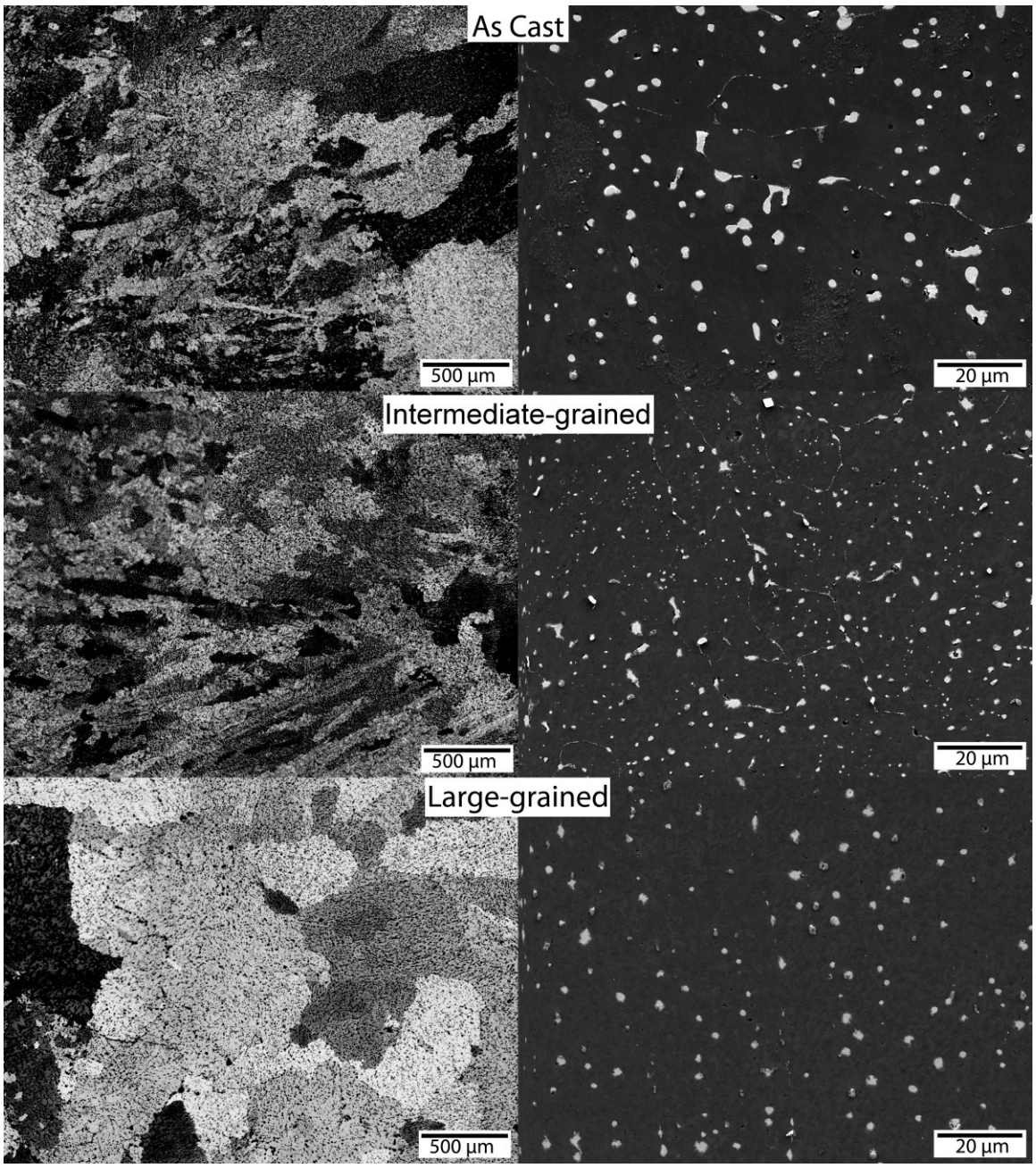

Figure 5. Optical (etched with Barker's reagent) and SEM micrographs of the Al-In conditions studied. Backscattered electrons interacting with the pole piece result in atomic weight contrast in the secondary electron images.

A summary of the AE detected as a function of particle location is shown in Figure 10. Specimens with higher area fraction indium on the grain boundaries exhibit more AE, as expected.

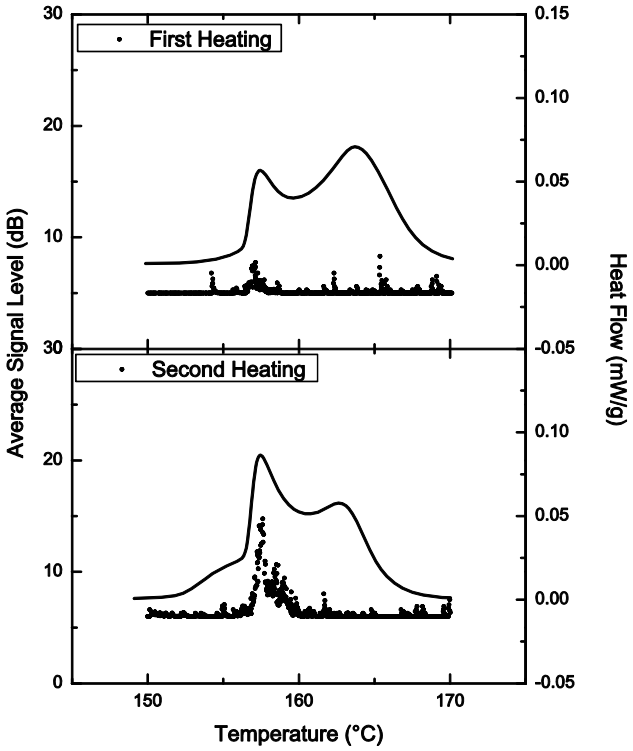

Figure 6. A comparison of DSC (line) and AE (scatter) for the first and second heating cycles of the intermediate-grained specimen.

As a final observation, the appearance of the melting point depression in Figure 6 may be evidence of the formation of metastable cubic indium, which would be expected to have a lower melting temperature. Cubic indium has been reported in melt-spun Al-In alloys by Van Aken and Fraser [38]. DSC of melt-spun ribbons with indium particles similar to that previously reported is shown in Figure 11 and shows three distinct melting distributions: metastable cubic indium, equilibrium melting of tetragonal indium, and the

elevated temperature melting of faceted cubic indium particles less than 30 nm in diameter.

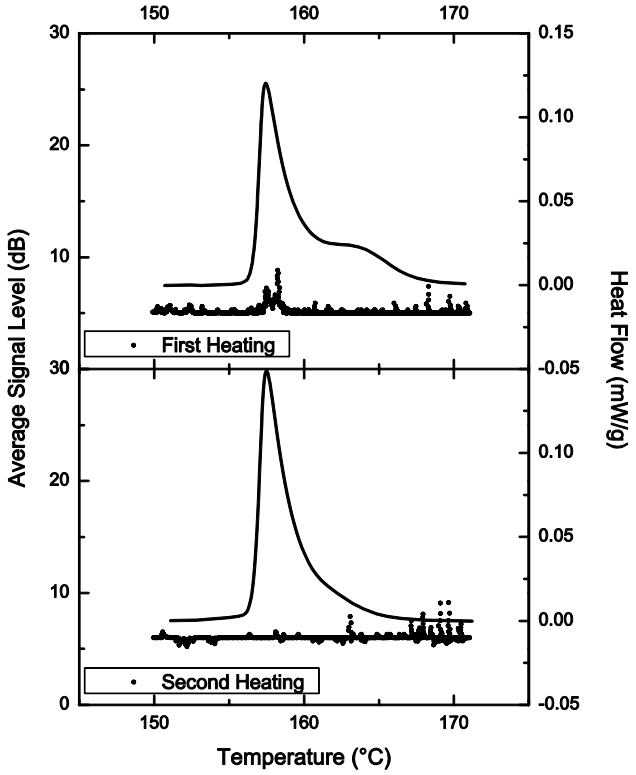

Figure 7. A comparison of DSC (line) and AE (scatter) for the first and second heating cycles of the large-grained specimen.

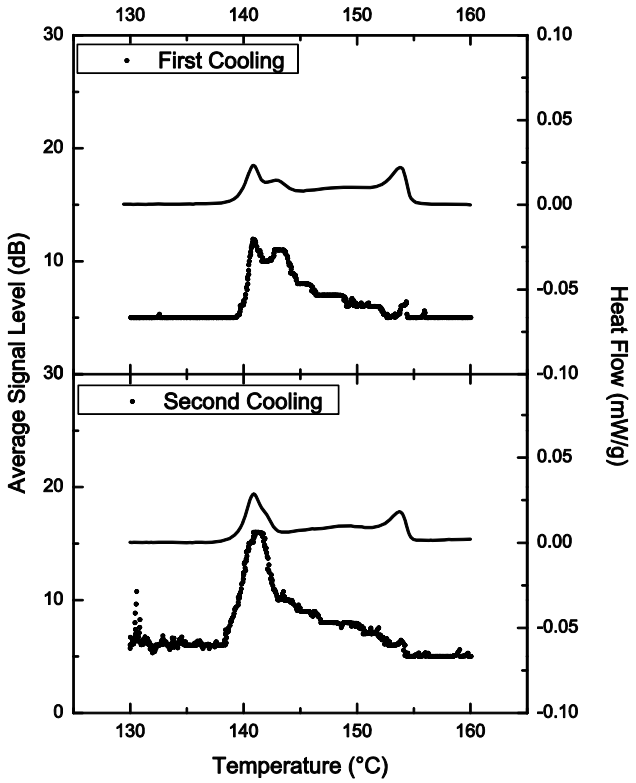

Figure 8. A comparison of DSC (line) and AE (scatter) for the first and second cooling cycles of the large-grained specimen.

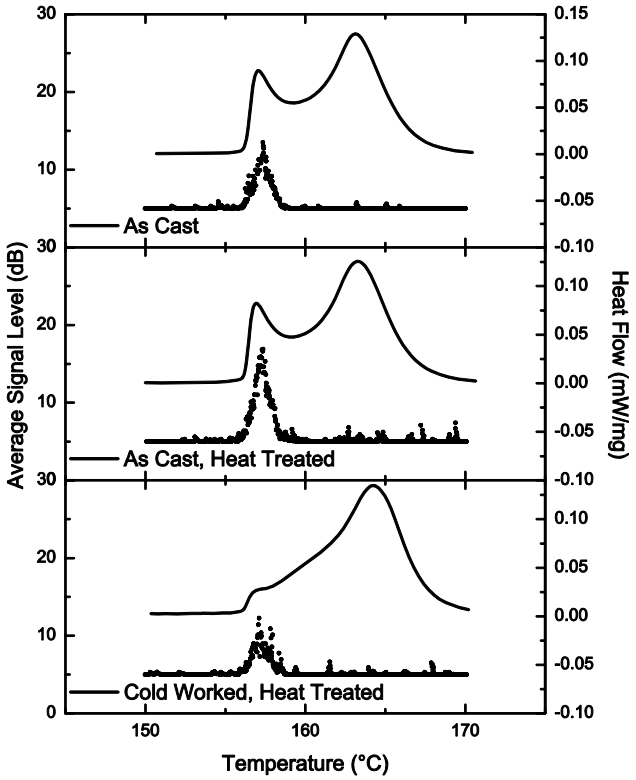

Figure 9. A comparison of DSC (line) and AE (scatter) in heating for the low-temperature anneal specimens.

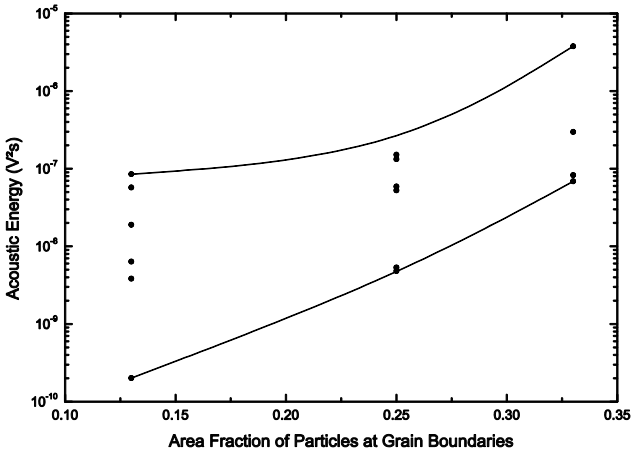

Figure 10. A summary of the acoustic energy as a function of the fraction of particles at grain boundaries.

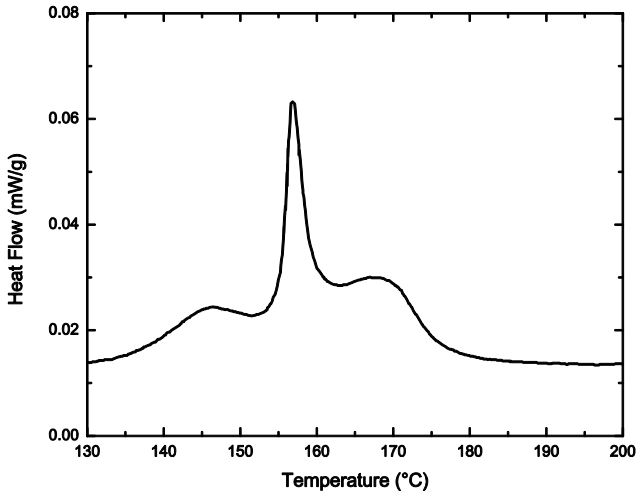

Figure 11. DSC of a melt-spun Al-12In alloy.

IV. DISCUSSION

The AE data must be considered in context of the relaxation mechanisms studied by Malhotra and Van Aken [13,21,25]. Malhotra and Van Aken have proposed that matrix relaxation time governs the melting temperature elevation, and Kuba and Van Aken have suggested that rapid relaxation mechanisms for melting particles produce AE through prismatic loop generation [32]. Consequently, particles associated with a short matrix relaxation time (on the order of 10^{-6} seconds) melt at the equilibrium temperature, and particles associated with a long matrix relaxation time (on the order of 10^{5} seconds) melt at elevated temperature [32]. Relaxation times were calculated based on diffusion of vacancies in aluminum and elastic parameters for the indium particle and aluminum matrix [22]. The distribution of melting temperatures is considered a distribution of matrix relaxation times [13]. Dislocation-based strain accommodation would be expected to be reversible and compatible with previous internal friction results. That is, the

alternating stress during the internal friction measurement affects the stability of the critical nucleus around the melting temperature, with compression stabilizing the solid phase and tension stabilizing the liquid phase.

The thermomechanical treatments and tests should be considered in context of dislocation annealing in aluminum, due to the temperature range overlap with the melting of indium. Frank and prismatic loops are established to anneal out between 100 and 200 °C, with elimination time as a function of temperature and loop size [39]. Prismatic loops are fully annealed after 10 minutes at 200 °C [40], and are very nearly annealed after 10 minutes at 193 °C [41]. Loretto et al. have annealed Frank loops at 138 °C for 20 minutes [36]. As an example of the effect of temperature, Edington and Smallman show Frank loops of nearly 0.5 μm in diameter disappear after about 4 minutes at 165 °C [42]. Vandervoort notes that long dislocation lines straighten, but do not anneal, at 200 °C and lower [40].

The larger AE peak and the larger equilibrium melting peak in the DSC data produced for the second cycle in Figure 6 suggest a shorter relaxation time as a result of multiple heating cycles. This agrees with previous DSC results which found less melting temperature elevation after the initial cycle and that the decrease in particle superheat did not change significantly after the second cycle [13]. Malhotra and Van Aken have shown that a small amount of cold work after repeated cycling produces a DSC distribution similar to the first scan [13]. An explanation is offered by Vandervoort; he shows 5% cold reduction will sweep out all dislocation loops in the material, decreasing the dislocation density and producing a structure similar to the original annealed condition [40]. Therefore, the presence of dislocation loops produced from the last cycle upon

cooling may account for the differences in AE and DSC on the second heating cycle. It follows that the cycle of dislocation generation on phase change and dislocation annealing during testing saturates after one test cycle.

For the large-grained specimens, multiple heating cycles decreases the AE detected in Figure 7. However, while previous results have shown proportional AE response for the equilibrium melting peak, the large equilibrium melting peak for the large-grained specimens is not associated with a large AE peak. The authors considered that cavitation during solidification might produce the AE seen in Figure 8 and account for the detection of AE across the whole solidification range. It should be emphasized, however, that superheating would not be possible in the presence of a void, since a liquid nucleus would perfectly wet the solid-vapor interface. AE would also be precluded by a void, as no matrix relaxation would be necessary for melting of the indium particle. If cavitation were responsible for the AE upon cooling, then the subsequent DSC scans upon heating should not produce superheating either. This is clearly not the case as shown by Figure 6. Malhotra and Van Aken have shown that a significant portion of particles still exhibit superheat even after six test cycles and that only the first cycle significantly changes the DSC scan [13].

Cavitation as a mechanism of AE was further tested by examining the thermodynamic restrictions on void formation during cooling. Following the analysis by Bourgeois et al. [43], the free energy barrier to void nucleation can be estimated by Equation 1. The surface energy, σ, is calculated as $\sigma = \sigma_v - \sigma_{\alpha\beta}/4$, where $\sigma_v = (\sigma_{v\alpha} + \sigma_{v\beta})/2$. The subscript v denotes a surface energy in vacuum, while α denotes the aluminum matrix and ß denotes the indium particle. Values for the surface energy

calculations were taken from de Boer [44]. The thermodynamic driving force for nucleation of a void, ΔG_V, is estimated as $k_B T \ln C_V/C_V^{eq}$, where k_B is Boltzmann's constant, T is absolute temperature of solidification, and C_V/C_V^{eq} is the ratio of actual to equilibrium vacancy concentration. Using Bourgeois's estimate of 10^6 for the vacancy supersaturation ratio results in a lower limit for the activation energy. A lower vacancy concentration would be expected for the slower cooling rate used in this study (0.4 C°/s as compared to 100-1000 C°/s). The volumetric strain energy misfit accommodated by the void, ΔG_S, is estimated to be the fraction volume change upon solidification of the indium particle, 0.025. Therefore, a lower bound for the activation energy of void nucleation, ΔG^*, can be estimated as 2.6 eV. Bourgeois comments that an activation energy of 0.027 eV would be expected to yield associated voids for 50% of the particles; thus, voids would not be expected to form on air-cooling Al-In from the solidification temperature.

$$\Delta G * = \frac{16\pi\sigma^3}{3(\Delta G_V - \Delta G_S)^2} \quad (1)$$

The analysis for void formation can be taken a step further by using the analysis of Tan et al. [45] for comparing formation energies of Frank dislocation loops, perfect prismatic dislocation loops, and voids. Figure 12 shows the comparison between activation energies for critical nuclei of the vacancy sinks. Perfect loops are more favorable than voids for low vacancy supersaturations ($C_V/C_V^{eq} < \sim 50$). Frank loops are more favorable than voids for the entire vacancy supersaturation range examined; however, Frank loops are also known to anneal in pure aluminum after 20 minutes at 138 °C [36]. Consequently, Frank loops would not be expected to remain at the solidification temperature, but if the specimen cools quickly enough, may be a viable vacancy

accommodation mechanism. Tan et al. also note that vacancy loops become more favorable than voids as the number of vacancies in the structure increases. Dislocation loop size is assumed to be a function of indium particle size [29], and void size would be expected to be a function of indium particle size as well, the relatively large particles examined in the present study would be expected to further stabilize vacancy loops.

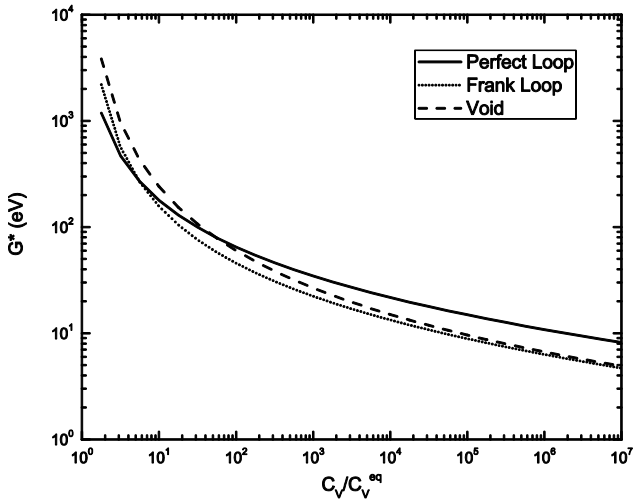

Figure 12. Activation energies for the nucleation of various vacancy sinks as a function of vacancy supersaturation. Calculations were performed at 156 °C.

However, void formation upon quenching from 500 °C to process the large-grained specimens may explain the lack of AE in heating seen in Figure 7, especially if the quench-related voids were large enough to remain after the first testing cycle. If the vacancy loss during quenching is taken to be negligible, the vacancy supersaturation can be estimated by the equilibrium vacancy concentrations at the processing temperature and room temperature. At 500 °C the vacancy concentration is calculated to be 1×10^{-4}, and

at 25 °C the vacancy concentration is calculated to be 1 x 10^{-11} [46]. Thus, a vacancy supersaturation of 1 x 10^{7} might be expected. Repeating Bourgeois's analysis in Equation 1 with the higher vacancy supersaturation and the elevated temperature results in calculated void activation energy that is comparable to the value calculated for Al-Sn. Void formation was observed after quenching for about 50 % of the particles in Al-Sn, despite a calculated activation energy above the theoretical limit [43]. Void formation is observed to be competitive with Frank loop generation in Figure 12 for high vacancy supersaturations ($C_V/C_V^{eq} > 10^6$) during solidification of the indium particles. Unfortunately, void presence cannot be examined by conventional metallographic preparation, as indium is often added to aluminum to prevent passivation of sacrificial anodes [47]. Consequently, the indium particles corrode during polishing and in air after polishing. As well, particle pull-out may also be an issue stemming from the low pressures used to polish the Al-In specimens.

The disproportionately large AE peak for undercooled solidification (relative to the DSC peaks and the rest of the AE curve) should be investigated in lieu of void formation during cooling tests. Simple particle solidification would not be expected to be the source of AE because the relationship between AE and DSC response is not constant. Particles experiencing undercooling can be considered similar to those experiencing superheat. The matrix is behaving rigidly during the solidification range, which would normally be indicative of a long relaxation time. However, the sudden AE peak at the most-undercooled solidification events suggests a rapid relaxation mechanism, when the matrix does finally relax. In contrast, the long relaxation time expected to produce the required constraint for particle superheat during melting does not exhibit AE. A

difference in the ability to nucleate dislocations is suggested to explain the AE observed for all solidifying indium particles, but not for superheated melting indium particles. In this case, the molten particle interface may act as a free surface during cooling. Conversely, the particle is solid and acts as a coupled surface during heating. Dislocations are easily annihilated at free surfaces; it follows that the reverse is also true. That is, the molten particle would act more like a free surface than an embedded particle, reacting similarly to dislocation-based growth of voids. The presence of disproportionately large AE suggests dislocation loop generation at the interface to quickly accommodate the solidifying particle.

Evidence for a dislocation mechanism to accommodate the volume change is provided by the 140°C annealing experiments where dislocation recovery is possible. Following an anneal, more dislocations are required to nucleate to accommodate the volume change during the melting transformation and an increase in AE was observed (see Figure 9). The removal of prior dislocation structures would also result in a longer slip distance for the newly-generated dislocations, and thus a stronger AE signal. In this case, the DSC does not change since the fraction of particles melting at the equilibrium temperature does not change. The increase in elevated melting temperature particles after cold working and low-temperature annealing suggests that the process resulted in shifting a number of particles to a slower relaxation mechanism. The decrease in AE confirms this. Grain rotation due to yielding in compression deformation would increase the fraction of low-angle grain boundaries that contain indium inclusions, which are expected to exhibit longer relaxation times [13]. The resulting dislocation network from cold-work

may also inhibit loop formation, decrease slip distance, and promote diffusional relaxation.

The analysis so far has concentrated on micron-sized indium particles. Literature establishes that both nanoparticle and bulk material melting are controlled by different mechanisms other than the strain-controlled transformation presented here. AE and matrix relaxation effects may only be present for a certain size range of particles. Interfacial effects for nanoparticles would be expected to control the reaction below this range. Conversely, indium particles would be expected to melt only at the equilibrium temperature as though they were bulk indium above this range. A size range can be established by considering the strain fields around a melting inclusion in an infinite matrix. Using the Eshelby inclusion model, the matrix strain surrounding an ideal spherical particle undergoing a volumetric transformation strain can be calculated, as derived by Bower [48]. A 50 nm radius particle melting with a dilation of 2.5% results in approximately one Burgers vector of elastic displacement in the aluminum matrix. Thus, we might expect a lower bound of 100 nm diameter particles to follow strain-dependent transformation and produce AE for rapid transformations.

Elastic accommodation of the critical radius of the molten indium nucleus can be considered as an upper bound. A particle large enough to elastically accommodate the volume expansion of the critical liquid nucleus would be expected to relax via diffusional mechanism and not exhibit AE, as the lifetime of the critical nucleus would be long. The radius of the critical nucleus is calculated to be 1.5 μm for a superheat of 0.1 °C. An indium particle of radius 9 μm would be expected to accommodate that nucleus with approximately one Burgers vector of displacement into the aluminum matrix.

Consequently, AE (as well as the superheat effect resulting from matrix constraint) is precluded for particles outside 0.1 to 18 μm in diameter.

It is worth noting that these strain-based calculations were performed using room-temperature data. Near the melting point of indium, the upper bound is expected to decrease significantly due to the easier accommodation of deformation at high temperatures. For the lower bound, more strain would be required to nucleate dislocations due to the decrease in Young's modulus, so the lower bound is expected to increase in size. Thus, a narrowing of the predicted range for AE is expected. Experimental verification of the necessary particle size for AE remains to be done.

Most solid state phase transformations produce a change in volume and the evidence presented for a dislocation-based accommodation of a volume change without the motion of an interface inspires curiosity into the possible dislocation density produced. Following the analysis of D.C. Ahn [29], the number of prismatic loops necessary for an average indium particle to melt can be calculated. For particles larger than approximately 400 times the Burgers vector (about 100 nm for aluminum), the analysis becomes simply geometric by treating multiple loops as a cylinder of material that is pushed away from the particle. That is, the volume change accommodated by each loop is $\pi r^2 b$, where r is the loop radius (estimated to be 75% of the particle radius) and b is the magnitude of the 1/2<110> Burgers vector for aluminum. The size of the necessary cylinder is then calculated as a multiple of the loop's Burgers vector. For the Al-17In alloy investigated in Materials Letters [32], 73 loops per average particle of 0.33 μm in radius are estimated to be necessary to accommodate the 2.5% volume expansion. If the whole 15.7 wt.% of indium transformed in this manner, the dislocation density would

increase by 4.1 x 10^9 cm^{-2}, which establishes an upper limit. In reality, at most half of the volume of particles typically melt at the equilibrium temperature and display acoustic emission indicative of dislocation formation. Portions of 10 to 20 % may be more applicable for some of the specimens presented here depending on the deconvolution of the DSC data used. A "typical" microstructure with a theoretical particle size of 1 μm in diameter at the monotectic composition in which 10 % of the particles melt at the equilibrium temperature and display AE would generate an increase in dislocation density of 3.5 x 10^8 cm^{-2}. For comparison, continuously cooled bainite is reported to generate a dislocation density of 1.7 x 10^{10} cm^{-2} [23]. Van Bohemen [12] has published AE data for continuously cooled bainite. The acoustic emission observed in Al-In and bainite in steels is comparable after normalizing for the volume transformed and the inherent differences in resistance between AE detection systems. The authors conclude that AE cannot be used as a criterion or descriptor of displacive transformations. Rather, any volumetric phase transformation with a short relaxation time may generate AE. In this case, an upper limit to the relaxation time of 10^{-6} seconds [32] to 5 x 10^{-5} seconds [13] serves as an estimate for AE detection. More sensitive AE systems may detect longer relaxation times.

Most solid state phase transformations are noted to be heterogeneously nucleated at grain boundaries. Classical nucleation theory would show that the critical volume of the nucleus is smaller at grain boundaries as a result of surface energy considerations and thus heterogeneous nucleation at grain boundaries has a kinetic advantage. The results of this AE study would suggest that the relaxation of the strain energy at the grain boundary plays as important a role as surface energy. Here the presence of the grain boundary

provides the rapid relaxation by nucleating dislocations to accommodate the volume strain of transformation. The significance of strain energy relaxation in nucleation might also be a function of temperature. In the present study, AE observed at the melting point of indium is 0.46 times the absolute melting temperature of pure aluminum, and at these temperatures dislocation recovery and removal of point defects are expected. It is thus interesting to note that for melting of lead embedded in copper the ratio is 0.44, which was studied via internal friction by Wolfenden and Robinson [34].

V. CONCLUSIONS

Dislocation emission was determined to be the cause of the observed AE in both heating and cooling in Al-In alloys. A size range for the presence of AE and the superheat effect was hypothesized to be 0.1 to 18 μm in diameter. Furthermore, liquid inclusions were suggested to act as a free surface within the higher-melting point matrix and promote dislocation generation during solidification of the indium particles. An upper limit to the dislocation density generated by rapid relaxation and strain accommodation in the aluminum matrix by melting of embedded indium particles was calculated as 4.1×10^{9} cm^{-2}. Comparisons to continuously cooled bainite suggests that acoustic emission should not be used as a criterion of displacive phase transformations. Any volume change associated with a diffusion controlled phase transformation may generate AE provided the relaxation of the product or parent phase occurs in less than 10^{-5} seconds. Strain energy may be as important as surface energy in terms of classical nucleation theory and grain boundary relaxation may explain the preference in nucleation along prior austenite grain boundaries in steel.

ACKNOWLEDGMENTS

This work was supported in part by the National Science Foundation, the Department of Energy, and the American Iron and Steel Institute under contract No. CMMI 0726888. The authors thank Eric Bohannan at the Missouri S&T Materials Research Center.

SECTION

2. CONCLUSIONS

AE was determined to be generated by plastic strain accommodation of a melting or solidifying embedded particle. A dislocation mechanism of prismatic dislocation loop punching was investigated to account for the matrix plasticity. A size range for detection of AE and observation of the superheat effect in this system due to melting and solidification of embedded indium particles was proposed to be 0.1 to 18 μm in diameter. Liquid inclusions were suggested to behave as free surfaces within higher-melting point matrices and to encourage dislocation generation during solidification of embedded particles. The dislocation density generated by rapid matrix relaxation and plastic strain accommodation of the melting indium particles was calculated to have an upper limit of 4.1×10^{9} cm^{-2}. As a result, the calculation implies acoustic emission should not be used as a criterion of displacive phase transformations due to comparisons with the dislocation density and acoustic emission generated by continuously cooled bainite. Even more so, any volume change associated with a diffusion controlled phase transformation may generate AE provided the relaxation of the product or parent phase occurs in less than 10^{-5} seconds. When the present results are considered in terms of classical nucleation theory, the data suggests that strain energy may be as important as surface energy. Easier relaxation at grain boundaries may describe the tendency to nucleate new phases at prior austenite grain boundaries in steel.

APPENDIX A.

LABVIEW CODE FOR ACOUSTIC EMISSION APPARATUS

National Instruments LabVIEW software was used to develop a data collection system for the present studies. LabVIEW was chosen for its ease of use and rapid development time due to the graphical, rather than textual, nature of the code. The code was executed in a sequential structure, as the Physical Acoustics PCI-2 acquisition card needed to be initialized and set-up before data collection could begin. The code is presented here as each sequential "frame."

The PCI-2 system is first initialized as seen in Figure A.1. In the next frame, shown in Figure A.2, the data collection settings are specified. In-depth information for various recommended settings for various applications can be found in Physical Acoustic's documentation for the LabVIEW drivers used to program the card. Frames 3, 4, and 5 are presented in Figure A.3. Frame 3 is used to turn on time-dependent features and set the time constants for measurements such as RMS voltage. It was also used to turn on recording of the detected waveforms in case the data was desired at a later point. Frame 4 checked the validity of the setup before continuing, and Frame 5 prepared the card to begin collecting data.

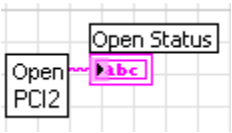

Figure A.1. The sub-VI used to initialize the PCI-2 system.

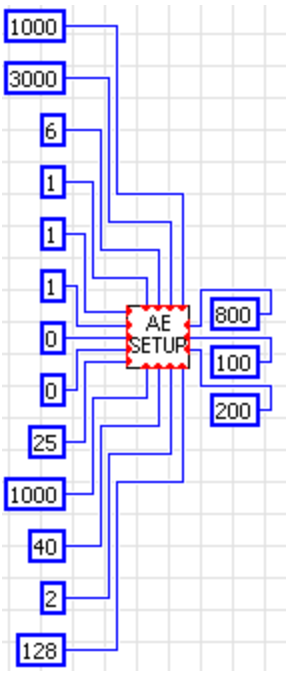

Figure A.2. The sub-VI used to set up the PCI-2 card and specify parameters.

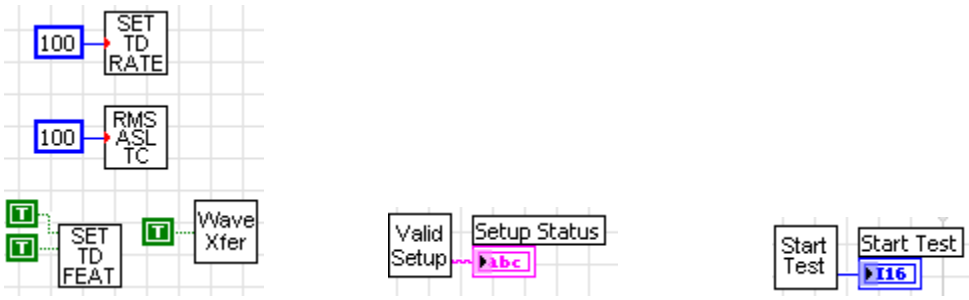

Figure A.3. The sub-VIs used to choose data modes, verify settings, and start the test.

Frame 6 contained several case structures used to probe the PCI-2 card's memory and construct an array of the desired data, which is then written to the hard disk. The general structure is shown in Figure A.4. The card is polled for which types of data it has in memory; the messages the card puts out determine which case is used. The outer

structure reads a value of either 1 or 0; 1 is a blank case used to keep the system idle while waiting for data. 0 contains an inner case structure that varies between an empty default structure, case 2, and case 173. For case 2, shown in Figure A.5, the system pulls the RMS voltage and average signal level from the card and combines it with time and temperature data acquired from a National Instruments USB-9129. This data is constructed into an array and written to a data file. For case 173, the program calls the waveform data from the card and compensates for the various gains and losses in the system, seen in Figure A.6. Each waveform above a certain threshold specified in Frame 2 is recorded in this manner and written to disk in its own separate file.

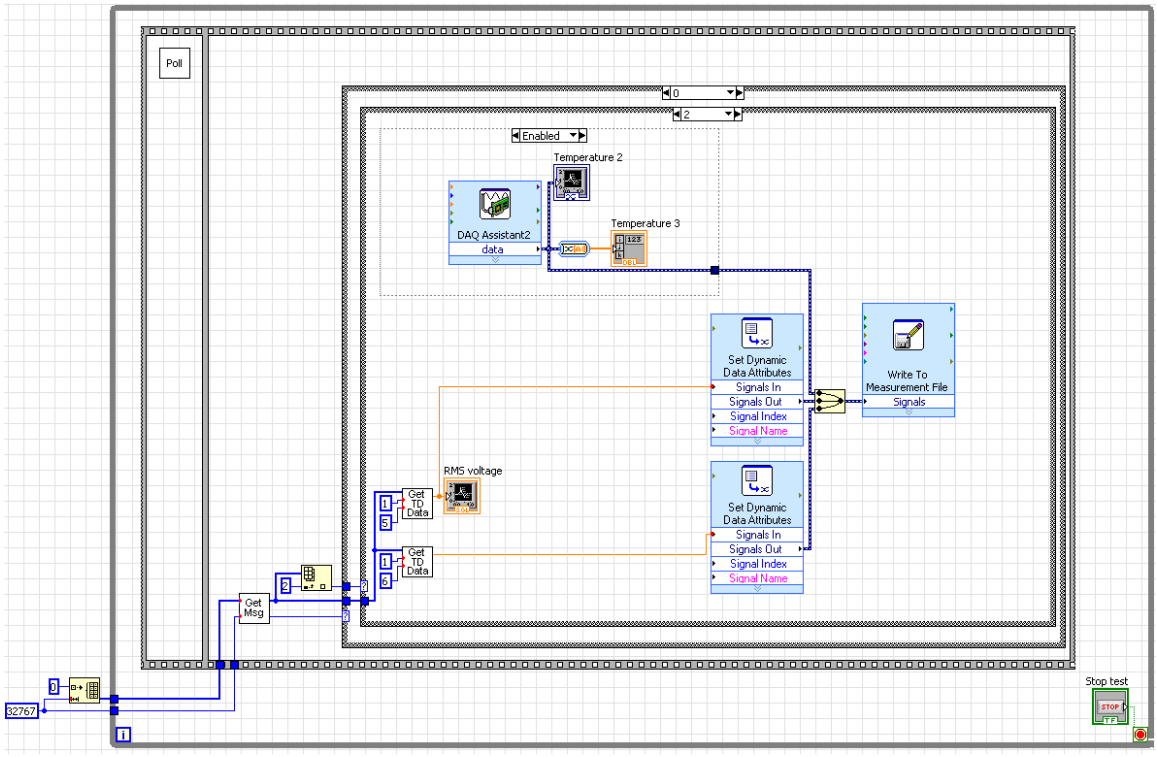

Figure A.4. The general structure of Frame 6. Case 0-2 is shown.

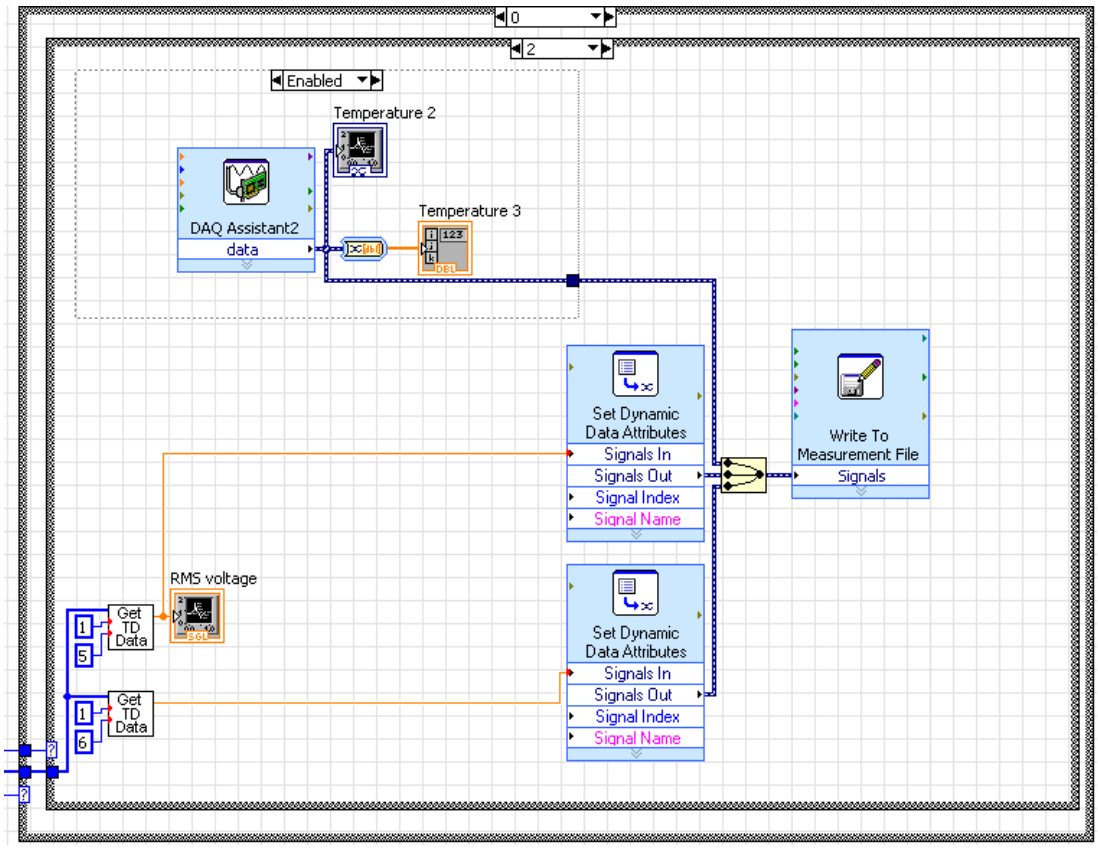

Figure A.5. The code used when the inner case structure has a value of 2.

Frame 6 also contains a stop button that begins the shutdown procedure at the end of the test. This portion of the code was written to ensure proper procedures are followed and any resource calls used by the card are released. Consequently, this stop button should always be used when ending the test, rather than the button built into LabVIEW. Frames 7 through 10 contain the shutdown procedure, shown in Figure A.7. The test is paused, and the memory of the PCI-2 card is called, read, and cleared until the card returns that it has no new data. The “Stop Test” sub-VI is called, and the connection to the PCI-2 card is closed.

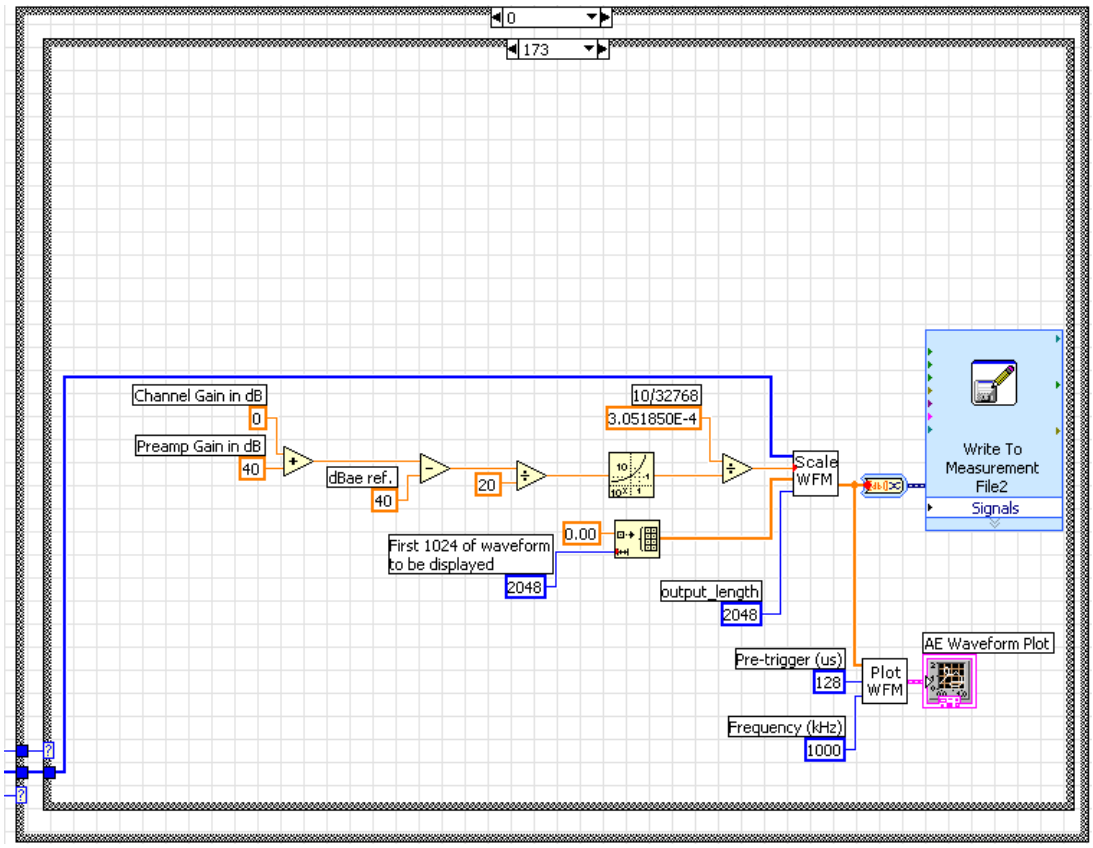

Figure A.6. The code used when the inner case structure has a value of 173.

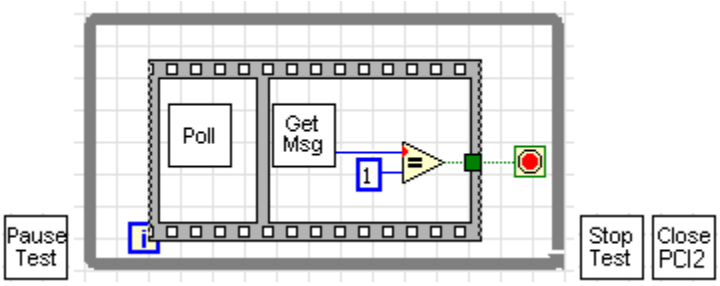

Figure A.7. The shutdown procedure for the PCI-2 system; Frames 7-10 are presented.

APPENDIX B.

SPHERICAL ESHELBY INCLUSION SOLUTION

The Eshelby inclusion model is an elegant and classic solution for the elastic stresses and strains surrounding an ellipsoidal particle undergoing a volume change associated with a transformation. The solution is performed as a thought experiment where the transforming region is removed from the matrix and allowed to transform unconstrained, resulting in free energy and volume changes. Surface tractions are applied between the particle and the matrix, and the particle is re-inserted into the matrix. Stresses between the particle and the matrix are allowed to come to equilibrium. The process is illustrated in Figure B.1.

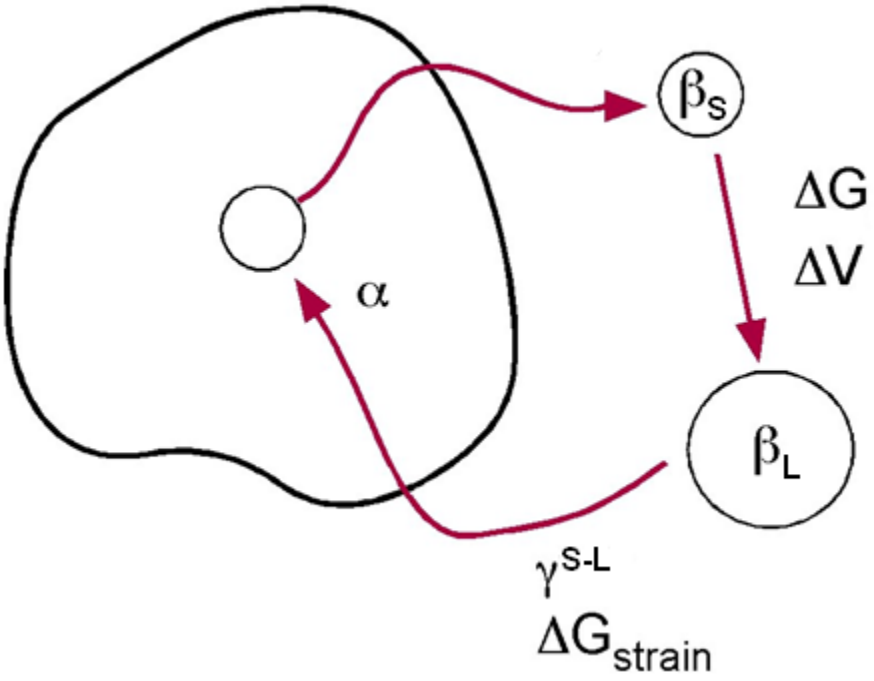

Figure B.1. An illustration of the steps taken to solve the Eshelby inclusion.

The original equations used by Eshelby are often described as formidable; many authors have published solutions for various configurations for ease of use. Bower [48] has provided a solution for the field outside a spherical inclusion using Papkovich-Neuber potentials. Bower's solution is recounted below, in Equations 2 and 3.

$$u_i = \frac{(1+v)a^3}{2(1-v)E}\left\{\frac{(2p_{ik}^T x_k + p_{kk}^T x_i}{15R^5}(3a^2 - 5R^2) + \frac{p_{jk}^T x_j x_k x_i}{R^7}(R^2 - a^2) + \frac{4(1-v)p_{ik}^T x_k}{3R^3}\right\} \quad (2)$$

$$\sigma_{ij} = \frac{a^3}{2(1-v)R^3}\left\{\begin{array}{c} \frac{p_{ij}^T}{15}\left(10(1-2v) + 6\frac{a^2}{R^2}\right) + \frac{p_{ik}^T x_k x_j + p_{jk}^T x_k x_i}{R^2}\left(2v - 2\frac{a^2}{R^2}\right) \\ + \frac{\delta_{ij} p_{kk}^T}{15}\left(3\frac{a^2}{R^2} - 5(1-2v)\right) + \frac{\delta_{ij} p_{kl}^T x_k x_l}{R^2}\left((1-2v) - \frac{a^2}{R^2}\right) \\ -\frac{x_i x_j p_{kl}^T x_k x_l}{R^4}\left(5 - 7\frac{a^2}{R^2}\right) + \frac{x_i x_j p_{kk}^T}{R^2}\left(1 - \frac{a^2}{R^2}\right) \end{array}\right\} \quad (3)$$

The equations were solved using a program written in Python 2.7; the code is printed below.

```
# Calculator to find displacements and stresses just outside a spherical Eshelby
inclusion
#
# Written by Michael Kuba

#import libraries
from sys import argv
import math

#material parameters
nu = 0.35 #poisson's ratio
E = 70*10**9 #young's modulus, pascals
e_kk = 3 * 0.008265 #sum of diagonals in transformation strain matrix
e_ij = dict() #transformation strain matrix
for i in range(1, 4): #building e_ij
  for j in range(1, 4):
    if i == j:
      e_ij[(i,j)] = 0.008265 #linear change is cube root of volume change
    else:
      e_ij[(i,j)] = 0
#a = 0.5 * 10**-6
a = float(raw_input("Specify radius in micrometers: ")) * 10**-6

#constants
k_delta = dict() #kronecker delta
for i in range(1, 4): #building k_delta
  for j in range(1, 4):
```

```
    if i == j:
      k_delta[(i,j)] = 1
    else:
      k_delta[(i,j)] = 0


x = dict() #coordiantes of point of interest in meters
#x[(1)] = 1 * 10**-6
x[(1)] = float(raw_input("Specify distance from center of inclusion in \
  micrometers: ")) * 10**-6
x[(2)] = 0
x[(3)] = 0


#functions
R = math.sqrt(math.fsum( [x[(i)]**2 for i in range(1,4)] ))
#distance from origin to point of interest

p_ij = dict() #defining p_ij
for i in range(1,4):
  for j in range(1,4):
    p_ij[(i,j)] = (E/(1 + nu)) * (e_ij[(i,j)] + \
      (nu * e_kk * k_delta[(i,j)] / (1-2*nu)))

#Separate einstein summations
pikxk = dict()
for i in range(1,4):
  pikxk[(i)] = math.fsum([p_ij[(i,k)]*x[(k)] for k in range(1,4)])
pkk = math.fsum([p_ij[(k,k)] for k in range(1,4)])

#piecewise definition of u_i in form: u_i = u_a * (u_b + u_c + u_d)
u_a = ((1 + nu) * a**3) / (2 * (1 - nu) * E)

def u_b(i):
  b = (2 * pikxk[(i)] + pkk * x[(i)]) * (3 * a**2 - 5 * R**2) / (15 * R**5)
  return b

def u_c(i):
  c = math.fsum([pikxk[(j)] * x[(j)] for j in range(1,4)]) * x[(i)] * \
    (R**2 - a**2) / (R**7)
  return c

def u_d(i):
  d = 4 * (1 - nu) * pikxk[(i)] / (3 * R**3)
  return d

def u_i(i):
  e = u_a * (u_b(i) + u_c(i) + u_d(i))
```

```
  return e

#piecewise definition of sigma_ij in the form:
#sigma_ij = sigma_a * (sigma_b + sigma_c ... + sigma_g)
sigma_a = a**3 / (2 * (1 - nu) * R**3)

def sigma_b(i,j):
  b = (p_ij[(i,j)] / 15) * (10 * (1 - 2 * nu) + 6 * a**2 / R**2)
  return b

def sigma_c(i,j):
  c = ((pikxk[(i)] * x[(j)] + pikxk[(j)] * x[(i)])/(R**2)) * (2*nu - 2 * a**2/R**2)
  return c

def sigma_d(i,j):
  d = k_delta[(i,j)] * pkk * (3 * a**2/R**2 - 5 * (1-2*nu)) / 15
  return d

def sigma_e(i,j):
  e = k_delta[(i,j)] * math.fsum([pikxk[(k)]*x[(k)] for k in \
    range(1,4)]) *((1-2*nu) - a**2/R**2) / R**2
  return e

def sigma_f(i,j):
  f = -1 * (x[(i)] * x[(j)] * math.fsum([pikxk[(k)]*x[(k)] for k in \
    range(1,4)]) * (5 - 7 * a**2/R**2) / R**4)
  return f

def sigma_g(i,j):
  g = x[(i)] * x[(j)] * pkk * (1 - a**2/R**2) / R**2
  return g

def sigma_ij(i,j):
  h = sigma_a * (sigma_b(i,j) + sigma_c(i,j) + sigma_d(i,j) + \
    sigma_e(i,j) + sigma_f(i,j) + sigma_g(i,j))
  return h

print "a = %r um" % (a * 10**6)
print "x = %r um" % (x[(1)] * 10**6)
for i in range(1,4):
  print "  u_%r = %r nm" % (i, round(u_i(i)*10**9,2)) #output in nm
for i in range(1,4):
  print "  sigma_(%r,%r) = %r MPa" % (i, i, \
    round(sigma_ij(i,i)*10**-6,2)) #output in MPa
```

APPENDIX C.

DISLOCATION DENSITY CALCULATION

D.C. Ahn [29,30] and Lubarda [31] have shown that rapid void growth at temperatures too low for diffusion to occur in the necessary time scale can be accomplished by dislocation emission. Specifically, they have evaluated punching of interstitial prismatic loops, which can be envisioned as a disc of interstitial atoms moving in a glide cylinder with height normal to the face of the disc. Because the stress conditions surrounding a transforming inclusion are similar to those around a void during tensile plasticity (i.e. hydrostatic), the analysis for void growth can be used for melting of indium particles. D.C. Ahn has performed an extensive derivation to find the plastic volume change associated with a pile-up of prismatic loops emitted from the void [29]; the result is shown in Equation 4, where $\Delta V_{pile\text{-}up}$ is the total plastic volume change, N is the number of loops emitted, ρ_o is the loop radius (taken to be 75% of the void starting radius), b is the matrix Burgers vector magnitude, and $\sum_{i=1}^{N} \Delta V^*(z_i)$ is the volume change associated with the elastic strains resulting from the loop's presence (and is negative).

$$\Delta V_{pile-up} = N\pi\rho_0^2 b + \sum_{i=1}^{N} \Delta V^*(z_i) \tag{4}$$

For voids larger than 400 times the Burgers vector, the negative elastic strains can be ignored. The problem then becomes simply geometric; each loop is treated as a disc of material being removed from the surface of the void. The number of loops per average particle can be calculated by finding the volume of the average particle and taking into account the 2.5% volume change on melting for indium. The number of average particles per unit volume in the specimen can be easily calculated by evaluating the volume fraction of second phase. Consequently, the number of loops per unit volume is known,

which can be transformed to dislocation density by summing the circumference of the loops. Specific numbers for reference are included in Paper 2.

This calculation establishes an upper limit to the dislocation density, as it computes a "geometrically necessary" number of dislocations to accommodate the transformation strain. It is apparent that not all of the particles transform via this mechanism, or the AE would be directly proportional to the DSC of the specimen, and superheated particles would exhibit AE. A more accurate estimation of dislocation density might be produced by deconvoluting the DSC scans and evaluating the volume fraction of indium melting at equilibrium. However, the AE generated during the equilibrium melting transformation is not always proportional to the equilibrium melting DSC peak. In fact, several other mechanisms may be present that allow particles to melt at equilibrium without matrix plasticity, such as voids at the particle-matrix interface. Further, the DSC scans may not always deconvolute to two Gaussian peaks; some of the DSC presented here appears to be the sum of three Gaussian distributions. As such, this calculation should be taken as a zeroth-order approximation.

APPENDIX D.

DISLOCATION DENSITY MEASUREMENT BY XRD

Strain broadening of the x-ray diffraction (XRD) line scan is well documented. Both the Williamson-Hall and Warren-Averbach analyses are used to quantify the line broadening effects in the diffraction peak profiles. However, Ungár et al. have shown that the conventional plots are inadequate to fully describe the strain effects in the matrix [49]. Ungár et al. have proposed modifying the Williamson-Hall and Warren-Averbach plots with a contrast factor, C, based on the diffraction vector, the line and Burgers vectors, and the elastic constants of the crystal. The plots are then referred to as the *modified* Williamson-Hall plot and the *modified* Warren-Averbach plot.

For either analysis, it is paramount that the data is pristine. The $K\alpha_2$ or $K\beta_2$ peaks must be removed if an elemental source is used. Negligible instrumental broadening is preferred. The analysis must be well-informed, i.e. the proper peak positions must be known. The data collected as θ or 2θ should be transformed to inverse space according to $K = 2\sin\theta/\lambda$, where lamda is the wavelength of x-rays. The full-width at half maximum (FWHM) can be calculated as $\Delta K = 2\cos\theta(\Delta\theta)/\lambda$, where Δθ is half of the FWHM.

The exact contrast factors can be calculated by hand, but for most applications, the average contrast factor can be used. More insight into contrast factors can be found in [50]. Average contrast factors can be calculated by hand following [50], but at the time of writing, a useful web-based calculator exists at http://metal.elte.hu/anizc/.

The Williamson-Hall plot is based on the form

$$\Delta K = \frac{0.9}{D} + \Delta K_D, \tag{5}$$

where ΔK_D is the strain contribution to peak broadening and D is the average grain or particle size. ΔK_D is evaluated according to

$$\Delta K_D = A(\rho^*)^{1/2} + A'(Q^*)^{1/2}. \tag{6}$$

The symbols ρ* and Q* refer to the "formal" dislocation density and "formal" fluctuation of the dislocation density. A and A' are constants determined by the outer cutoff radius of dislocations, R_e, and the auxiliary parameters R_1 and R_2. The full Williamson-Hall equation is derived as

$$\Delta K = \frac{0.9}{D} + \sqrt{\frac{\pi A b^2}{2}}\sqrt{\rho}\left(K\bar{C}^{1/2}\right) + \frac{\pi A' b^2}{2}\sqrt{Q}(K^2\bar{C}), \quad (7)$$

where ρ and Q become "real" values, and b is the Burgers vector. As observed by the equation, the modified Williamson-Hall method should be plot the FWHM in terms of ΔK against $KC^{1/2}$. A quadratic regression then gives the coefficients of each term.

As of this writing, Ungár has not fully characterized the meanings of all the variables necessary to complete the Williamson-Hall analysis and only the average particle size can be computed. Until R_1 and R_2 are interpreted physically, the Warren-Averbach analysis is recommended for computing dislocation density. The Warren-Averbach analysis uses the real coefficients of the Fourier transform of the diffraction peak profiles. For continuous functions, the n-th real Fourier coefficient is given by

$$A_n = \int_{-\frac{a}{2}}^{\frac{a}{2}} f(x)\cos\left(2\pi n\frac{x}{a}\right)dx, \quad (8)$$

where a is the width of the domain of the function in x. The Fourier transform can be discretized and performed on the line scan information accordingly. The n-th real coefficient is then given by

$$A_n = \frac{1}{a}\sum_{x=-a/2}^{a/2}\frac{I}{I_{max}} * \cos\left(2\pi n\frac{x}{a}\right) * \Delta x, \quad (9)$$

where I is the intensity of the diffraction profile, x is the diffraction angle in θ, Δx is the measurement interval in θ, and a is the width of the peak measurement. Care should be taken that each peak is cropped to a similar width, and that θ is normalized such that the center of the peak is at zero.

The traditional Warren-Averbach method plots the natural log of the Fourier coefficients against K^2. The *modified* Warren-Averbach method incorporates the contrast factor by plotting against K^2C. Ungár et al. have derived the *modified* Warren-Averbach equation as

$$\ln A(L) \cong \ln A^S(L) - \frac{\pi\rho b^2 L^2}{2}\ln\left(\frac{R_e}{L}\right)(K^2\bar{C}) + \frac{\pi^2 Q b^4 L^4}{4} ln\left(\frac{R_1}{L}\right)\ln\left(\frac{R_2}{L}\right)(K^2\bar{C})^2, \qquad (10)$$

where $L = na_3$, $a_3 = \lambda/2(\sin\theta_2 - \sin\theta_1)$, and $(\theta_2 - \theta_1)$ is the angular range of the measured diffraction profile. R_e, R_1, R_2, ρ, Q, and b maintain the same meanings as above. A^S refers to the size contribution, i.e. it refers to the particle size. The Fourier coefficients should be grouped by n values, e.g. in an FCC system, the first Fourier coefficients for the 111, 220, 200, 222, 311, and 400 peaks are all in one data set, and then the second Fourier coefficients are in a separate set. Values of n can be plotted as high as is feasible. Quadratic regression of each set of Fourier coefficients allows for solving of the equation, since it will be of the form above. The end result resembles Figure D.1, taken from Ungár [51].

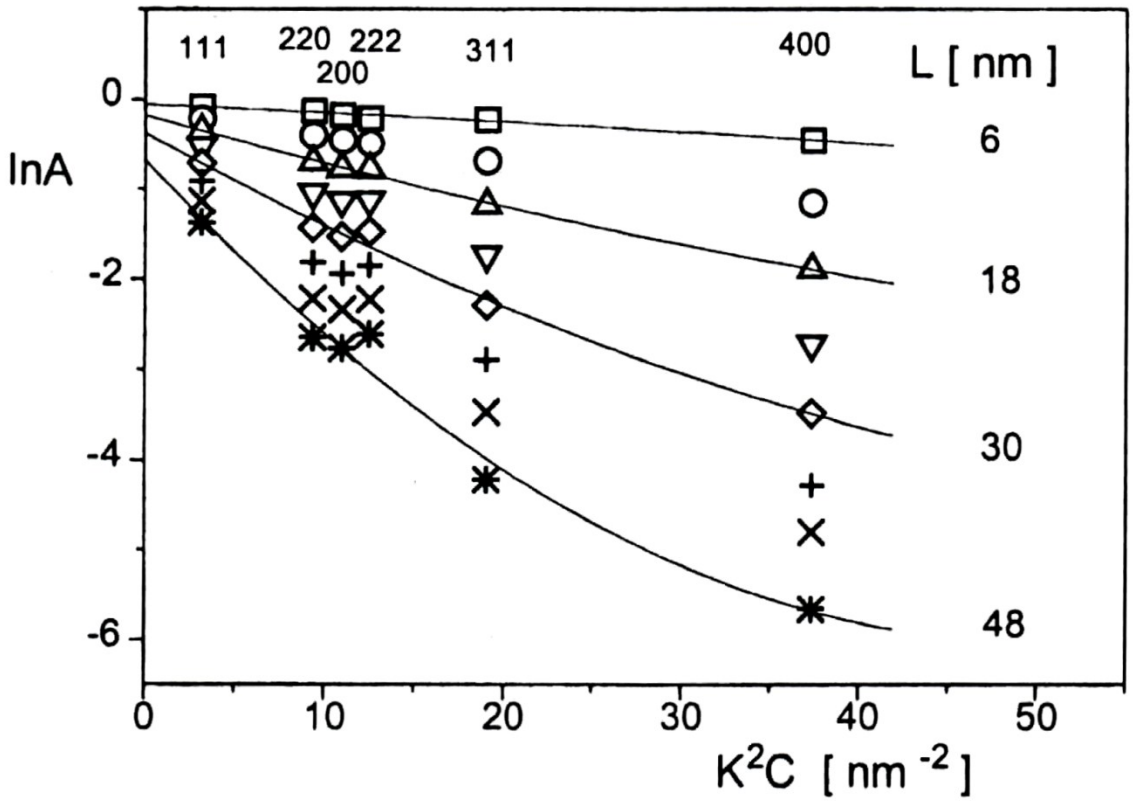

Figure D.1. An example plot of the *modified* Warren-Averbach analysis.

BIBLIOGRAPHY

[1] Standard Terminology for Nondestructive Examinations. 2009, ASTM E 1316 - 09a.

[2] Speich, G.R. and Fisher, R.M. “Acoustic Emission during Martensite Formation.” [ed.] R G Liptai, D O Harris, and C A Tatro. *Acoustic Emission (ASTM STP 505)*. Philadelphia: American Society for Testing and Materials, 1972, pp. 140-151.

[3] Van Bohemen, S.M.C.; Hermans, M.J.M.; and Den Ouden, G. “Acoustic emission monitoring of bainitic and martensitic transformation in medium carbon steel during continuous cooling.” Materials Science and Technology, Vol. 18, 2002, pp. 1524-1528.

[4] Clapp, P.C. “How Would we Recognize a Martensitic Transformation if it Bumped into us on a Dark & Austy Night?” Journal de Physique IV, Vol. 5, 1995, pp. 11-19.

[5] Voronenko, B.I. “Acoustic emission during phase transformation in alloys.” Metal Science and Heat Treatment, Vol. 24, Issue 8, 1982, pp. 545-553.

[6] Purvis, A.L.; Kannatey-Asibu Jr., E.; and Pehlke, R.D. “Linear discriminant function analysis of acoustic emission signals generated during solidification.” Transactions of the American Foundryman Society, Vol. 103, 1996, pp. 1-8.

[7] Tensi, H.M. “Acoustic emission measurements during crystallization and melting of metals and binary alloys.” Second Acoustic Emission Symposium Proceedings, 1974, pp. 46-57.

[8] Vorontsov, V.B. and Katalnikov, V.V. “Analysis of acoustic emission effect accompanying metal crystallization.” Journal of Physics: Conference Series, Vol. 98, Issue 052005, 2008, pp. 1-6.

[9] Frederick, J.R. and Felbeck, D.K. “Dislocation Motion As a Source of Acoustic Emission.” [ed.] R.G. Liptai, D.O. Harris, and C.A. Tatro. *Acoustic Emission (ASTM STP 505)*. Philadelphia: American Society for Testing and Materials, 1972, pp. 129-139.

[10] Mummery, P.M.; Derby, B.; and Scruby, C.B. “Acoustic Emission from Particulate-Reinfornced Metal Matrix Composites.” Acta Metallurgica et Materialia, Vol. 41, Issue 5, 1993, pp. 1431-1445.

[11] Landy, R.J. and Ono, K. “Acoustic emission behavior of a low alloy steel.” Journal of Acoustic Emissions, Vol. 1, Issue 1, 1982, pp. 7-19.

[12] Van Bohemen, S.M.C.; Hermans, M.J.M.; den Ouden, G.; Richardson, I.M. "A study of acoustic emission energy generated during bainite and martensite formation." Journal of Physics D: Applied Physics. Vol. 35, 2002, pp. 1889-1894.

[13] Malhotra, A.K. and Van Aken, D.C. "On the effect of matrix relaxation during the melting of embedded indium particles." Philosophical Magazine A, Vol. 71, Issue 5, 1995, pp. 949-964.

[14] Rösner, H.; Scherer, T.; and Wilde, G. "Electron tomography of lead nano-inclusions in aluminum." Scripta Materialia, Vol. 60, 2009, pp. 168-170.

[15] Allen, G.L.; Gile; W.W.; and Jesser, W.A. "The melting temperature of microcrystals embedded in a matrix." Acta Metallurgica, Vol. 28, 1980, pp. 1695-1701.

[16] Uhlmann, D.R. "On the internal nucleation of melting." Journal of Non-Crystalline Solids, Vol. 41, 1980, pp. 347-357.

[17] Saka, H.; Nishikawa, Y.; and Imura, T. "Melting temperature of In particles embedded in an Al matrix." Philos. Mag. A, Vol. 57, 1988, pp. 895-906.

[18] Couchman, P.R. and Jesser, W.A. "Thermodynamic theory of size dependence of melting temperature in metals." Nature, Vol. 269, 1977, pp. 481-483.

[19] Zhang, D.L. and Cantor, B. "Heterogeneous nucleation of In particles embedded in an Al matrix." Philosophical Magazine A, Vol. 62, Issue 5, 1990, pp. 557-572.

[20] Däges, J.; Gleiter, H.; and Perepzko, J.H. "Phase Transitions in Condensed Systems--Experiments and Theory." Materials Research Society Symposium Proceedings. Vol. 57, 1987, p. 67.

[21] Malhotra, A.K. and Van Aken, D.C. "An Internal Friction Study of Melting in Aluminum-Indium and Aluminium-Lead Alloys." [ed.] V.K. Kinra and A. Wolfenden. *M3D: Mechanics and Mechanisms of Material Damping (ASTM STP 1169).* Philadelphia: American Society for Testing and Materials, 1992, pp. 262-281.

[22] Malhotra, A.K. and Van Aken, D.C. "Experimental and theoretical aspects of internal friction associated with the melting of embedded particles." Acta Metallurgica et Materialia, Vol. 41, Issue 5, 1993, pp. 1337-1346.

[23] Bhadeshia, H.K.D.H. *Bainite in Steels*. London: IOM Communications, 2001. p. 29.

[24] Aaronson, H.I.; Spanos, G.; and Reynolds Jr, W.T. "A progress report on the definitions of bainite." Scripta Materialia, Vol. 47, 2002, pp. 139-144.

[25] Malhotra, A.K. and Van Aken, D.C. “Characterization of Room-Temperature Damping in Aluminum-Indium Alloys.” Metallurgical Transactions A, Vol. 24, 1993, pp. 1611-1619.

[26] Van Bohemen, S.M.C.; Sietsma, J.; Hermans, M.J.M.; Richardson, I.M. “Kinetics of the martensitic transformation in low-alloy steel studied by means of acoustic emission.” Acta Materialia, Vol. 51, Issue 14, 2003, pp. 4183-4196.

[27] Koike, J.; Miki, K.; Maruyama, K.; Oikawa, H. “Influence of liquid-phase inclusion on high-temperature deformation behavior in Al-Bi alloys.” Materials Science and Engineering A, Vols. 234-236, 1997, pp. 525-528.

[28] Huang, J.; Hsiung, L.M.; and Nieh, T.G. “Effect of strain rate on the elevated-temperature tensile properties of an Al-Pb alloy.” Scripta Materialia, Vol. 35, Issue 8, 1996, pp. 919-924.

[29] Ahn, D.C.; Sofronis, P.; and Minich, R. “On the micromechanics of void growth by prismatic-dislocation loop emission.” Journal of the Mechanics and Physics of Solids, Vol. 54, 2006, pp. 735-755.

[30] Ahn, D.C.; Sofronis, P.; Kumar, M.; Belak, J.; and Minich, R. “Void growth by dislocation-loop emission.” Journal of Applied Physics, Vol. 101, Issue 063514, 2007, pp. 1-6.

[31] Lubarda, V.A.; Schneider, M.S.; Kalantar, D.H.; Remington, B.A.; and Meyers, M.A. “Void growth by dislocation emission.” Acta Materialia, Vol. 52, 2004, pp. 1397-1408.

[32] Kuba, M.M. and Van Aken, D.C. “Plastic strain accommodation and acoustic emission during melting of embedded particles.” Materials Letters, Vol. 77, 2012, pp. 89-92.

[33] Galeski, A.; Koenczoel, L.; Piorkowska, E.; Baer, E. “Acoustic emission during polymer crystallization.” Nature, Vol. 352, 1987, pp. 40-41.

[34] Wolfenden, A. and Robinson, W.H. “Mechanical Damping in Leaded and in Lead-free Alpha Brass.” Acta Metallurgica, Vol. 25, 1977, pp. 823-826.

[35] Vyletel, G.M.; Krajewski, P.E.; Van Aken, D.C.; Jones, J.W.; and Allison, J.E. “Effect of Cold Work on the Recrystallized Grain Size in a Particle-Reinforced Aluminum Alloy.” Scripta Metallurgica et Materialia, Vol. 27, Issue 5, 1992, pp. 549-554.

[36] Loretto, M.H.; Clarebrough, L.M.; and Humble, P. “The Nature of Dislocation Loops in Quenched Aluminum.” Philosophical Magazine, Vol. 13, Issue 125, 1996, pp. 953-961.

[37] Haynes, W.M. and Lide, D.R. [ed.]. CRC Handbook of Chemistry and Physics. [Internet Version]. CRC, 2011.

[38] Van Aken, D.C. and Fraser, H.L. "Monotectic Solidification in Rapidly Solidified Al-In Alloys." International Journal of Rapid Solidification, Vol. 3, 1988, pp. 199-222.

[39] Dobson, P.S.; Goodhew, P.J.; and Smallman, R.E. "Climb Kinetics of Dislocation Loops in Aluminium." Philosophical Magazine, Vol. 16, Issue 139, 1967, pp. 9-22.

[40] Vandervoort, R. and Washburn, J. "On the Stability of the Dislocation Substructure in Quenched Aluminium." Philosophical Magazine, Vol. 5, Issue 49, 1960, pp. 24-29.

[41] Kroupa, F.; Silcox, J.; and Whelan, M.J. "On the Annealing of Prismatic Dislocation Loops in Aluminium." Philosophical Magazine, Vol. 6, Issue 68, 1961, pp. 971-978.

[42] Edington, J.W. and Smallman, R.E. "Faulted Dislocation Loops in Quenched Aluminium." Philosophical Magazine, Vol. 11, Issue 114, 1965, pp. 1109-1123.

[43] Bourgeois, L.; Bougaran, G.; Nie, J.F.; and Muddle, B.C. "Voids formed from solidifying tin particles in solid aluminum." Philosophical Magazine Letters, Vol. 90, Issue 11, 2010, pp. 819-829.

[44] de Boer, F.R.; Boom, R.; Mattens, W.C.M.; Miedema, A.R.; and Niessen, A.K. *Cohesion in Metals*. North-Holland: Elsevier Science Publishers B.V., 1988, p. 676.

[45] Tan, T.Y.; Plekhanov, P.; and Gösele, U.M. "Nucleation barrier of voids and dislocation loops in silicon." Applied Physics Letters, Vol. 70, 1997, p. 1715.

[46] von Guérard, B.; Peisl, H.; and Zitzmann, R. "Equilibrium Vacancy Concentration Measurements on Aluminum." Applied Physics A, Vol. 3, Issue 1, 1974, pp. 37-43.

[47] Gurrappa, I. "Cathodic protection of cooling water systems and selection of appropriate materials." Journal of Materials Processing Technology, Vol. I66, 2005, pp. 256-267.

[48] Bower, A.F. *Applied Mechanics of Solids*. CRC Press, 2010, pp. 294-299.

[49] Ungár, T.; Ott, S.; Sanders, P.G.; Borbély, A.; and Weertman, J.R. “Dislocations, grain size and planar faults in nanostructured copper determined by high resolution x-ray diffraction and a new procedure of peak profile analysis.” Acta materialia, Vol. 46, Issue 10, 1998, pp. 3693-3699.

[50] Ungár, T.; Dragomir, I.; Révész, Á.; and Borbély, A. “The contrast factors of dislocations in cubic crystals: the dislocation model of strain anisotrophy in practice.” Journal of Applied Crystallography, Vol. 32, 1999, pp. 992-1002.

[51] Ungár, T. “Dislocation densities, arrangements and character from X-ray diffraction experiments.” Materials Science and Engineering A, Vols. 309-310, 2001, pp. 14-22.

VITA

Michael Kuba was born in Kansas City, MO. He received his B.S. in Metallurgical Engineering from Missouri University of Science and Technology in May 2010 having attended since August 2006. He remained at Missouri University of Science and Technology to pursue an M.S. in Metallurgical Engineering under Dr. David C. Van Aken through August 2012.